



**HAL**  
open science

## Insights into B-Mg-Metasomatism at the Ranger U Deposit (NT, Australia) and Comparison with Canadian Unconformity-Related U Deposits

Joséphine Gigon, Roger G Skirrow, Matthieu Harlaux, Antonin Richard, Julien Mercadier, Irvine R Annesley, Johan Villeneuve

► **To cite this version:**

Joséphine Gigon, Roger G Skirrow, Matthieu Harlaux, Antonin Richard, Julien Mercadier, et al.. Insights into B-Mg-Metasomatism at the Ranger U Deposit (NT, Australia) and Comparison with Canadian Unconformity-Related U Deposits. *Minerals*, 2019, 9 (7), pp.432. 10.3390/min9070432 . hal-02334093

**HAL Id: hal-02334093**

**<https://hal.science/hal-02334093>**

Submitted on 25 Oct 2019

**HAL** is a multi-disciplinary open access archive for the deposit and dissemination of scientific research documents, whether they are published or not. The documents may come from teaching and research institutions in France or abroad, or from public or private research centers.

L'archive ouverte pluridisciplinaire **HAL**, est destinée au dépôt et à la diffusion de documents scientifiques de niveau recherche, publiés ou non, émanant des établissements d'enseignement et de recherche français ou étrangers, des laboratoires publics ou privés.

Article

# Insights into B-Mg-Metasomatism at the Ranger U Deposit (NT, Australia) and Comparison with Canadian Unconformity-Related U Deposits

Joséphine Gigon <sup>1,\*</sup>, Roger G. Skirrow <sup>2</sup>, Matthieu Harlaux <sup>3</sup>, Antonin Richard <sup>1</sup>, Julien Mercadier <sup>1</sup>, Irvine R. Annesley <sup>1</sup> and Johan Villeneuve <sup>4</sup>

<sup>1</sup> Université de Lorraine, CNRS, GeoRessources Lab, F-54500 Vandœuvre-lès-Nancy, France

<sup>2</sup> Geoscience Australia, Cnr Jerrabomberra Avenue and Hindmarsh Drive Symonston ACT, GPO Box 378, Canberra, ACT 2601, Australia

<sup>3</sup> Department of Earth Sciences, University of Geneva, Rue des Maraîchers 13, CH-1205 Geneva, Switzerland

<sup>4</sup> CRPG, UMR 7358 CNRS-UL, 15 rue Notre Dame des Pauvres, F-54501 Vandœuvre-lès-Nancy, France

\* Correspondence: josephine.gigon@univ-lorraine.fr

Received: 13 June 2019; Accepted: 11 July 2019; Published: 14 July 2019



**Abstract:** The Ranger deposit (Northern Territory, Australia) is one of the largest uranium deposits in the world. Uranium mineralisation occurs in crystalline basement rocks and is thought to belong to the unconformity-related category. In order to address the sources of magnesium and boron, and the temperature of the fluids related to boron and magnesium metasomatism that occurred shortly before and during the main uranium stage, in situ analyses of chlorite and tourmaline were carried out. The chemical composition of tourmaline shows an elevated X-site vacancy and a low  $Fe_{tot}/(Fe_{tot} + Mg)$  ratio typical of Mg-foitite. Uranium-related chlorite has relatively low Fe content (0.28–0.83 *apfu*) and high Mg content (3.08–3.84 *apfu*), with  $Si/Al = 1.08–1.22$  and  $Mg/(Mg + Fe_{tot}) = 0.80–0.93$  indicating a composition lying between the clinocllore and Mg-amesite fields. Chlorite composition indicates crystallisation temperature of 101–163 °C. The boron isotopic composition of tourmaline shows a range of  $\delta^{11}B$  values of ~1–9‰. A model is proposed involving two boron sources that contribute to a mixed isotopic signature: (i) evaporated seawater, which is typically enriched in magnesium and boron ( $\delta^{11}B \sim 40\text{‰}$ ), and (ii) boron from the crystalline basement ( $\delta^{11}B \sim -30$  to  $+10\text{‰}$ ), which appears to be the dominant source. Collectively, the data indicate similar tourmaline chemistry but significant differences of tourmaline boron isotopic composition and chlorite chemistry between the Ranger deposit and some of the Canadian unconformity-related uranium deposits. However, litho-geochemical exploration approaches based on identification of boron- and magnesium-enriched zones may be usefully applied to uranium exploration in the Northern Territory.

**Keywords:** tourmaline; chlorite; boron isotopes; metasomatism; unconformity-related uranium deposits; Ranger

## 1. Introduction

Unconformity-related uranium (U) deposits occur mainly in or close to the unmetamorphosed Proterozoic Athabasca and Thelon basins (Saskatchewan and Nunavut, Canada) and the McArthur Basin (Northern Territory, Australia). They are located in the vicinity of the intersection between the basin/basement unconformity and multiply-reactivated basement-rooted faults and are currently accounting for ~25% of the world U production [1–3]. Multiple mineralisation/remobilisation episodes have been identified in the three areas spanning over one billion years from ~1780 Ma for the primary diagenetic-hydrothermal mineralisation in Australian deposits [4] to more recent (<300 Ma) low-temperature remobilisation by meteoric fluids in Canadian deposits (e.g., [5]). Based on fluid

inclusion and stable isotope studies, the mineralising fluids are widely accepted to be 100–200 °C basinal brines, which underwent significant modification by interaction with basement lithologies [6–20]. Halogen geochemistry of fluid inclusions indicates that the basinal brines were produced by evaporation of seawater [9,21–24]. In addition to basinal brines, a low-salinity fluid of possible meteoric origin was also involved at the time of U deposition in the Australian deposits [9,10].

One typical feature of unconformity-related U deposits is the strong Mg-chlorite alteration and associated magnesium enrichment (i.e., Mg-metasomatism) in the vicinity of the ore zones [4,25–29]. In the Athabasca Basin, another proximal indicator for U mineralisation is Mg-rich tourmaline alteration and the associated boron enrichment (i.e., B-metasomatism) [27,29]. However, to our knowledge, there is no description of tourmaline alteration in U deposits from the Thelon area. Moreover, tourmaline alteration appears to be far less important in Australian deposits when compared to the Athabasca Basin [4,25,30].

Based on lithochemical, trace elements and stable isotope investigations, several models have been proposed for the sources of Mg and B enrichment in the ore zones, involving evaporated-seawater, evaporites, detrital tourmaline and basement rocks [4,29,31–33]. Thanks to large isotopic fractionation between different reservoirs, B isotopes in tourmaline are well suited for deciphering the source(s) of boron (e.g., seawater, evaporites, magmatic rocks, etc.) in the mineralising fluids and their relative proportions [32–34]. Using the world class Ranger deposit, we present a detailed investigation of the conditions for B-Mg-metasomatism in Australian unconformity-related U deposits [4]. In situ analysis of tourmaline and chlorite was used to elucidate the source(s) of B and Mg as well as the temperature of the fluids related to B-Mg-metasomatism that occurred shortly before and during the main U stage. The chemical composition of chlorite and tourmaline was determined by Electron Probe Microanalyses (EPMA) and the B isotopic composition of tourmaline was determined by Secondary Ion Mass Spectrometry (SIMS). The results are discussed in the frame of a systematic comparison with previous data obtained on Canadian and Australian unconformity-related U deposits highlighting the similarities and the differences between these mineral systems, as well as the consequences for U exploration.

## 2. Geological Setting of the Ranger Uranium Deposit

The Ranger deposit is one of the world's largest uranium deposits with resources estimated at 155.17 Mt of ore grading 0.09%  $U_3O_8$  with past production of 49,194 t  $U_3O_8$  from the Ranger 1 No 3 ore body [35] and 60,961 t of  $U_3O_8$  from the Ranger 1 No 1 ore body [36]. The Ranger 1 deposit is one of several large unconformity-related uranium deposits in the Alligator Rivers Uranium Field (ARUF, Figure 1), including the Jabiluka, Nabarlek and Koongarra deposits [37]. Most of the known major uranium deposits in the ARUF are hosted by pre-McArthur Basin metasedimentary basement rocks (Figure 1). The oldest basement in the ARUF is composed of ~2670–2510 Ma granite and gneiss, including the Nanambu Complex to the west of the Ranger and Jabiluka deposits [38–41]. The Neoproterozoic rocks are unconformably overlain by, or in faulted contact with, ~2020 Ma to ~1870–1860 Ma continental to marine basinal and volcanic rocks of the Woodcutters Supergroup and then by the Cahill Formation and Nourlangie Schist. The Cahill Formation comprises siliciclastic to pelitic schists (including uncommon, thin carbonaceous units), carbonate and calc-silicate rocks and amphibolites, and is the host sequence for the Ranger, Jabiluka and several other uranium deposits in the ARUF. The Nimbuwah orogenic event at ~1865–1855 Ma resulted in metamorphism to medium grade in the ARUF, and was accompanied by deformation and granitoid intrusions of the Nimbuwah Suite [38,40,41]. A tourmaline-bearing pegmatite at the Ranger deposit records zircon U-Pb ages of  $1867.0 \pm 3.5$  Ma and  $1862.8 \pm 3.4$  Ma and a monazite U-Pb age of  $1847 \pm 1$  Ma [42]. The zircon ages are interpreted to represent igneous crystallization during the Nimbuwah event, whereas the monazite age may record a later igneous or hydrothermal event that is also represented by mafic dykelets and veins at Ranger [4]. In the Pine Creek Orogen to the southwest of the ARUF, volcanism and renewed basin formation at

~1829–1825 Ma (Edith River Group, El Sherana Group) was accompanied and outlasted by intrusive magmatism of the Cullen Suite and Jim Jim Suite between ~1835 and ~1818 Ma [38].

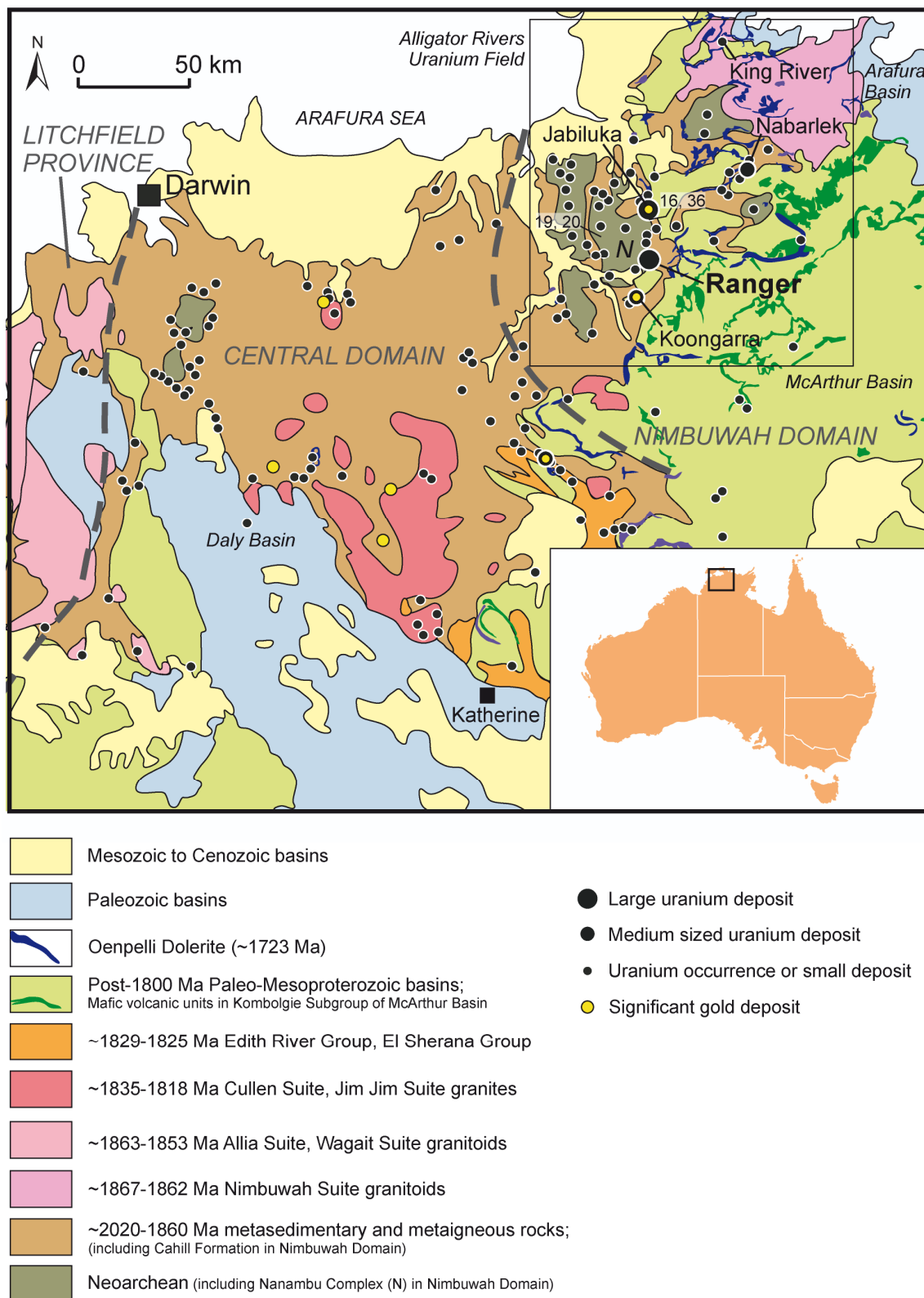


**Figure 1.** Location and geology of the Pine Creek Orogen comprising the Nimbuwah, Central and Litchfield Domains, and the location of the Ranger deposit and other uranium and gold deposits and occurrences within the Alligator Rivers Uranium Field (labelled box). After Skirrow et al. [4].

At the Ranger 1 deposit, the Cahill Formation comprises variably altered pelitic to psammitic and locally carbonaceous schists of the Upper Mine Sequence (UMS) and Hangingwall Schist (HWS), which overlie the carbonate-rich Lower Mine Sequence (LMS, Figure 2). The spatial distributions of rock types and whole-rock geochemical patterns at the No 3 orebody were described by Potma et al., Fisher et al. and Pevely et al. [26,43,44]. Most uranium mineralisation occurs within the UMS in zones enriched in Mg, Cu, Au and Ni, and depleted in Na, Ba, K and Ca. Mineralisation extends to more than 500 m depth in the eastern Ranger 1 No 3 Deeps Zone where it tends to be more Cu-rich and terminates against a major north-trending fault [26,43]. In the Deeps Zone relatively high-grade uranium mineralisation (e.g., 7 m at 1.3%  $U_3O_8$  [45]) occurs mainly within brecciated UMS rocks and in zones of complex faulting. Further details of alteration, geochemistry, zoning, mineralisation, and structure at the Ranger Number 1 orebody including the Deeps Zone are given by Skirrow et al., Fisher et al. and Pevely et al. [4,26,44]. Pre-ore silicification and/or quartz veining/infilling is present at most if not all of the major uranium deposits in the ARUF as replacements of carbonate rocks (Ranger, Jabiluka), near the Oenpelli Dolerite (Nabarlek) or as silicified fault zones (Koongarra). The fluids that originated the alteration halo and U mineralisation were highly-saline (>20 wt.% equivalent NaCl) NaCl-rich and  $CaCl_2$ -rich basinal brines, that mixed at the deposit with a low-salinity fluid, according to fluid inclusion studies [9,30,46]. The NaCl-rich and  $CaCl_2$ -rich brines are considered to share a common origin, i.e., evaporation of seawater at the surface of the McArthur Basin, but then underwent different physico-chemical modifications due to different percolation pathways and fluid/rock interactions in the basin/basement environments [9]. The temperatures of formation for unconformity-related U deposits of the Pine Creek Orogen range between 100 and 300 °C, based on the illite and chlorite geothermometers and fluid inclusion studies [10,30,46,47].

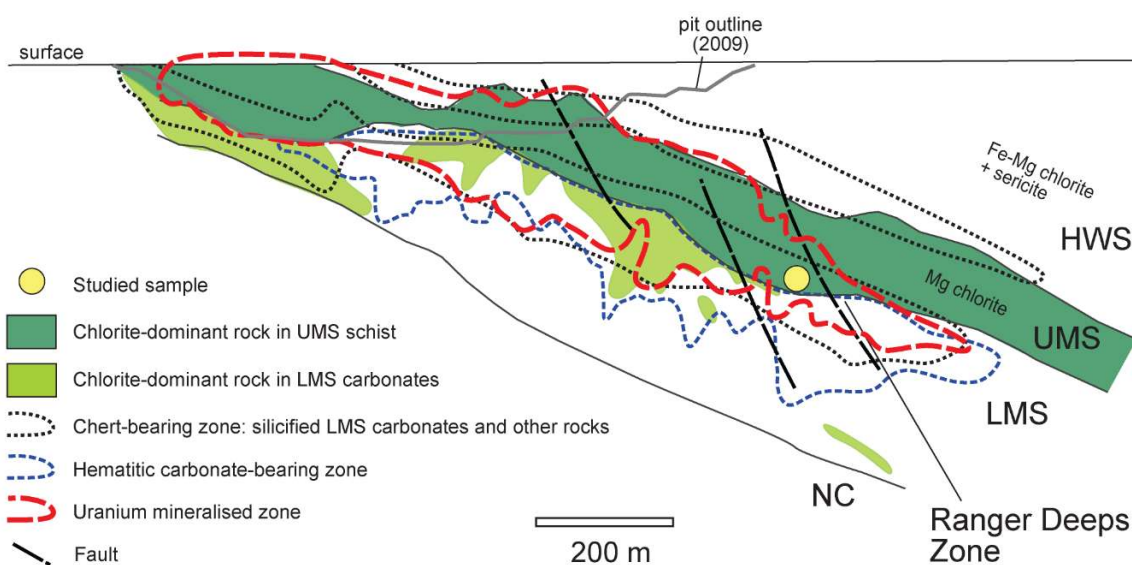


**Figure 2.** Generalised east–west cross sections of lithology, alteration and location of the sample investigated, at the Ranger 1 No 3 orebody (Australia). Modified from Skirrow et al. [4]. UMS: Upper Mine Sequence; LMS: Lower Mine Sequence; HWS: Hangingwall Schist.

### 3. Paragenetic Sequence and Tourmaline Occurrence

A detailed paragenetic sequence for the Ranger 1 deposit is presented in Skirrow et al. [4] and a simplified version, adapted to the focus of the present study (i.e., Mg-tourmaline and Mg-chlorite), is shown in Figure 3. The following descriptions are also taken from Skirrow et al. [4]. The first tourmaline generation in the area is of magmatic origin occurring in tourmaline-bearing pegmatite (not shown in Figure 2; see Skirrow et al. [4] for description). The pegmatite is massive, yet also sericitised and chloritised. Formation of magmatic tourmaline is constrained by zircon U-Pb ages at  $1867.0 \pm 3.5$  Ma and  $1862.8 \pm 3.4$  Ma [4]. Tourmaline-bearing pegmatites cross-cut the main tectonic fabric and are composed of quartz, K-feldspar, muscovite, tourmaline, apatite and zircon.

Characteristics	medium grade met.	retrograde alteration	pre-ore B1 breccia	pre-ore silicification	main stage uraninite	late uraninite
Age / timing	~1865 Ma	~1800 Ma	~1720-1680 Ma?	~1720-1680 Ma?	~1720-1680 Ma?	~1400? & ~475 Ma
Regional event	Nimbuwah	Shoobridge	← Kombolgie Fm			
Deformation	D1, ductile-brittle	D2, brittle-ductile	brittle: breccia B1	brittle: veins, breccia B2	brittle: breccia B3	brittle: veining
quartz	metamorphic + Q1 vein		dissolution	Q2	dissolution	Q3
carbonate				dissolution		
chlorite		Chl1 (Fe-Mg)	Chl2 (Mg)		Chl3 (Mg-Fe)	
white mica / clay		sericite		fine muscovite		
tourmaline	magmatic			T1 Mg-foitite	T2 Mg-foitite	
pyrite		? ? ?				
uraninite				early U1	U1	U2 U3
disordered carbon						

**Figure 3.** Simplified paragenetic sequence of the Ranger U deposit (Australia) with a focus on the successive generations of tourmaline, chlorite, quartz and uraninite (after Skirrow et al. [4]). Here, chemical and boron isotopic analyses were carried out on tourmaline T1 and chemical analyses were carried out on chlorite Chl2.

Two generations of hydrothermal tourmaline are documented, both associated with deformational events (veining and/or brecciation, Figure 4A) postdating the formation of the McArthur Basin. Early hydrothermal tourmaline T1 is coeval with quartz Q2, fine-grained muscovite, pyrite, the earliest uraninite early-U1 (dated at  $1688 \pm 46$  Ma [4], Figure 4B), and the dissolution of carbonate (Figure 3). This hydrothermal mineral assemblage corresponds to the pre-ore silicification event (Figure 3) which is interpreted to have occurred between ~1720 Ma and ~1680 Ma. Tourmaline T1 is acicular, forming fine-grained needles up to 5  $\mu\text{m}$  in width and 100  $\mu\text{m}$  in length, often radiating, intergrown with chlorite Chl2 and quartz Q2 (Figure 5). Tourmaline T2 is coeval with chlorite Chl3, pyrite and uraninite U1. In this study, only tourmaline T1 and chlorite Chl2 were investigated for their chemical and isotopic composition. Tourmaline T2 and chlorite Chl3 are too intimately intergrown and of such small grain size that the tourmaline T2 could not be analysed without contamination, even by in situ methods.

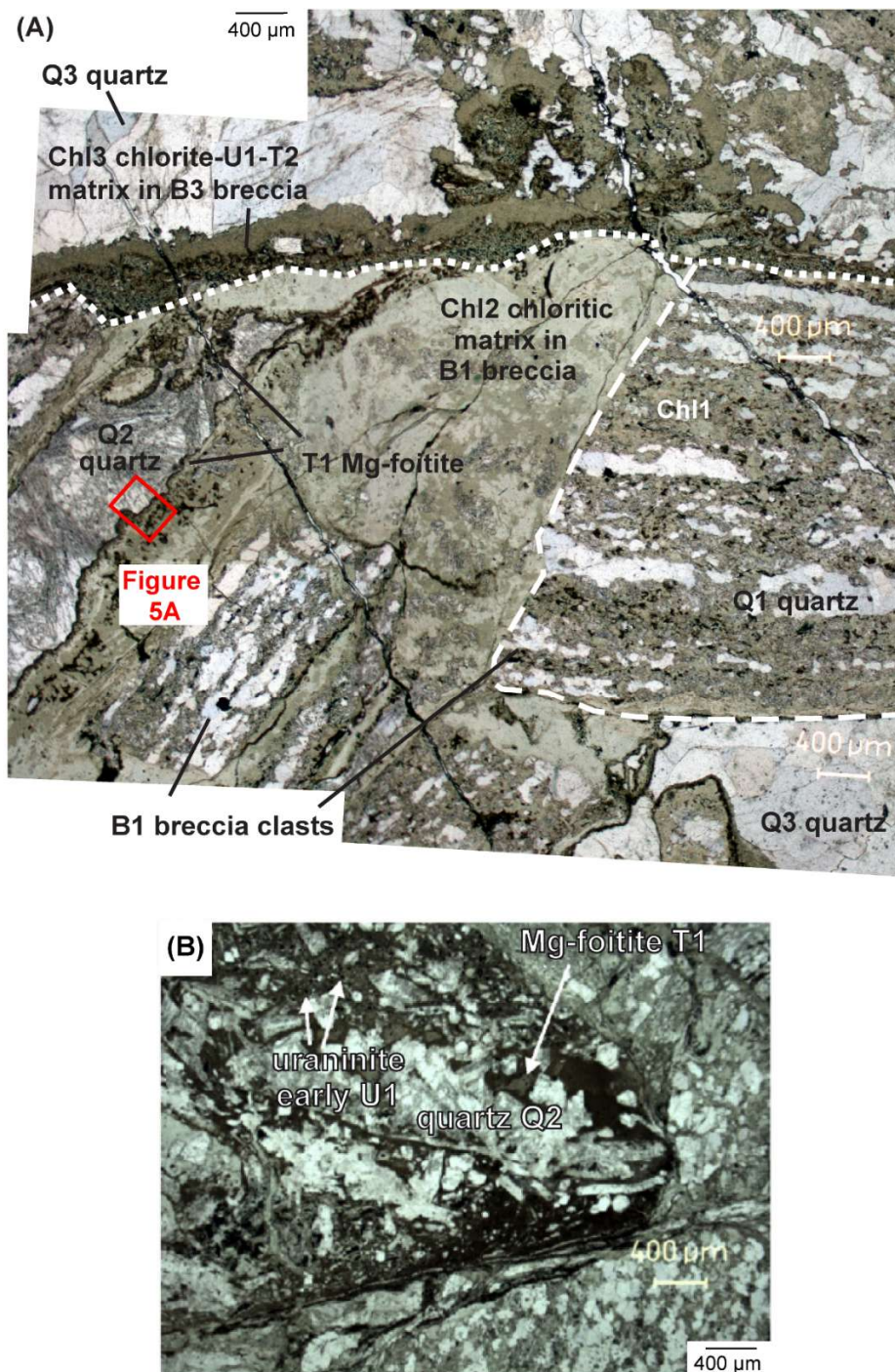


**Figure 4.** Chlorite-tourmaline-quartz generations and assemblages at the Ranger U deposit (Australia), from Skirrow et al. [4]. (A) Thin section studied for boron isotopes and major elements showing pre-ore B1 breccia, pre-ore silicification and main U1 ore stage. B1 breccia is composed of lithic clasts of banded quartz Q1 and chlorite Chl1 within a matrix of chlorite Chl2 and chlorite Chl3 that corrodes quartz. Some voids in B1 breccia are lined by tourmaline T1 and filled by quartz Q2 corresponding to the pre-ore silicification stage and B2 breccia. Both the B1 breccia and Q2-T1 assemblages were cut by ore-stage B3 breccia, with infill by chlorite Chl3, tourmaline T2, and uraninite U1. Voids in the B3 breccia matrix were filled by quartz Q3. Sample from drillhole S3PD759 402.9 m, transmitted light, from Skirrow et al. [4]. (B) Clast in B3 breccia containing intergrowths of euhedral quartz Q2, brownish fine-grained tourmaline T1, and fine-grained disseminated uraninite U1. Sample from drillhole S3PD759 395.3 m, transmitted light, from Skirrow et al. [4].

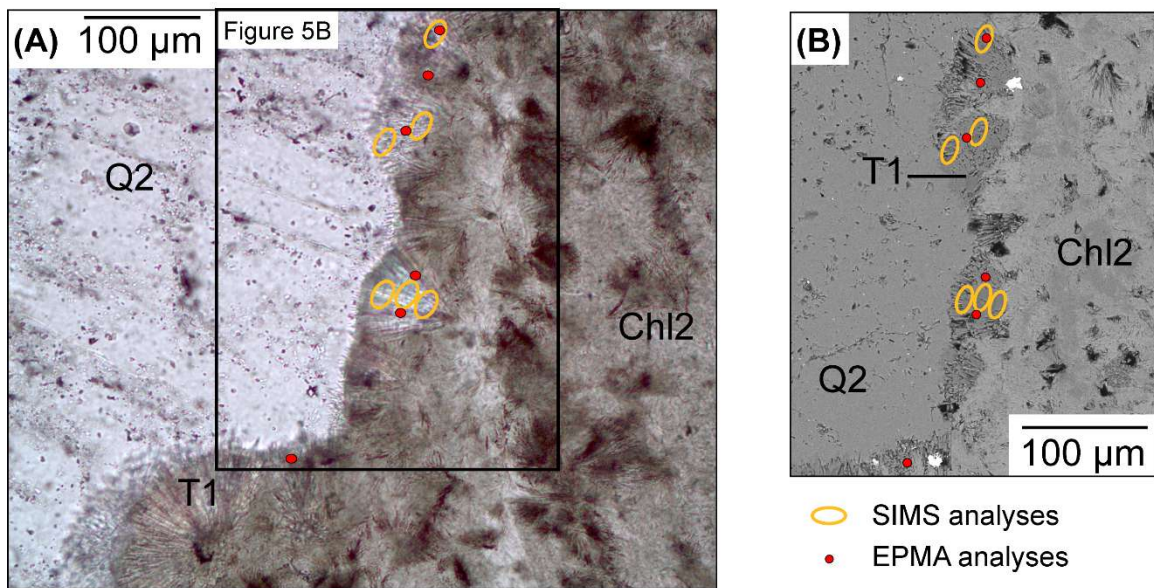


**Figure 5.** Zoom on the pre-ore silicification minerals from the Ranger U deposit (Australia): chlorite Chl2, on which very fine-grained rosettes of tourmaline T1 grow, then cemented by quartz Q2 with locations of the EPMA (red dots) and SIMS (orange ellipses) in situ analyses on tourmaline T1; (A) transmitted light. (B) BSE image. Sample from drillhole S3PD759 402.9 m.

**4. Materials and Methods**

Analytical work was completed on a single, representative polished thin section (DDH: S3PD759, 402.9 m) collected from the chlorite-dominant Upper Mine Sequence schists and within the uranium mineralised zone, in close proximity to the main fault zone (Figure 2). The distribution of the major elements and B isotope analyses in tourmaline T1 and major elements on chlorite Chl1 and Chl2 is illustrated in Figure 6. For scanning electron microscopy and electron probe microanalyses the entire thin section was carbon coated, and for secondary ion mass spectrometry half of the thin section was cut and gold coated.

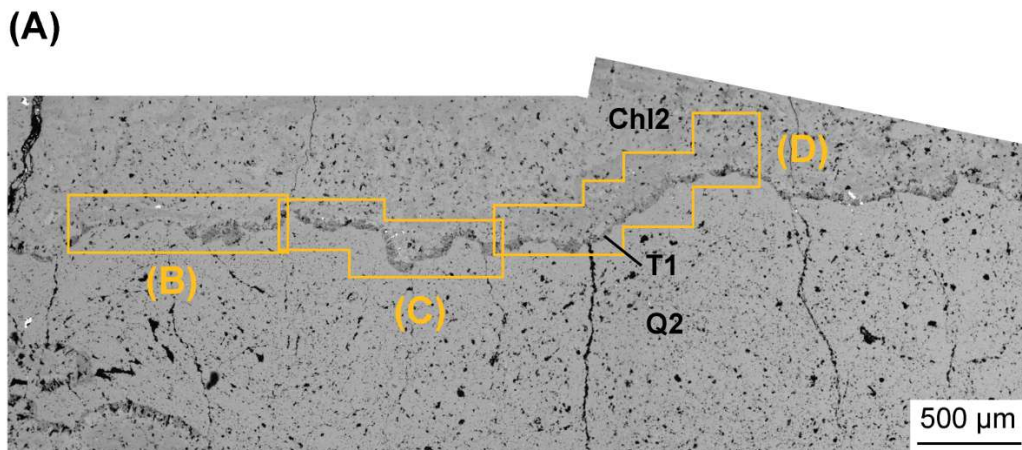


**Figure 6.** Cont.

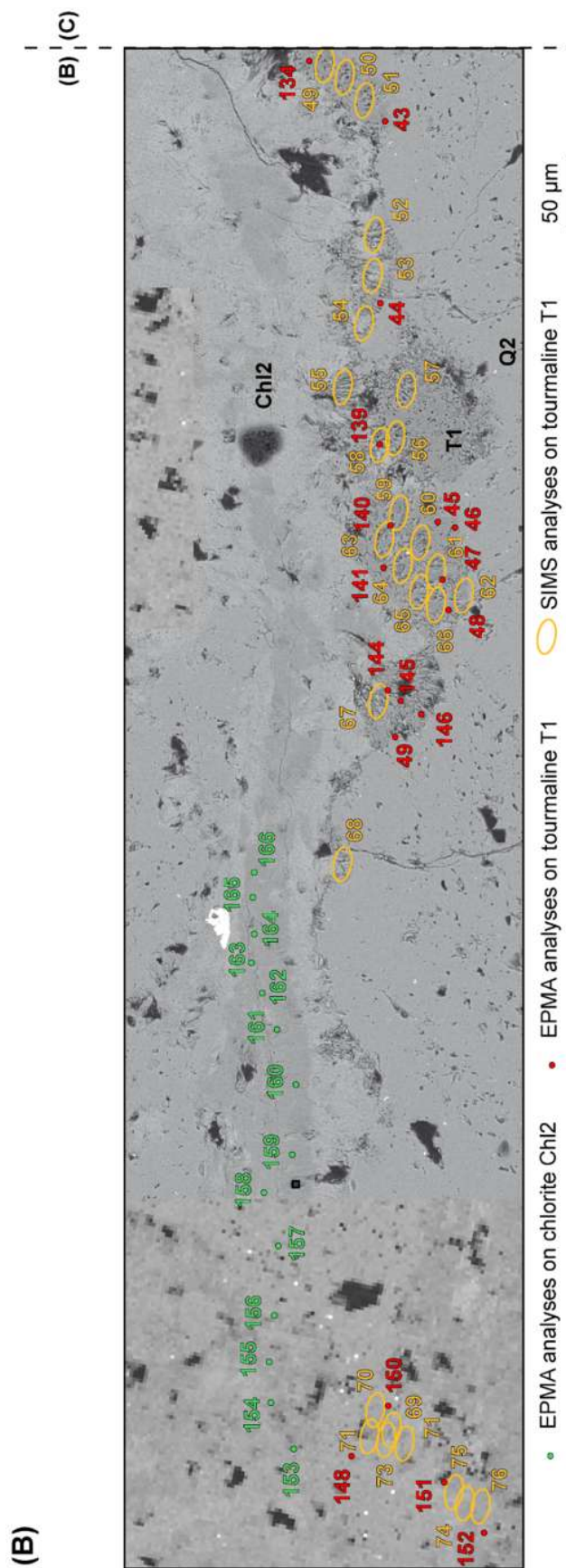


Figure 6. Cont.

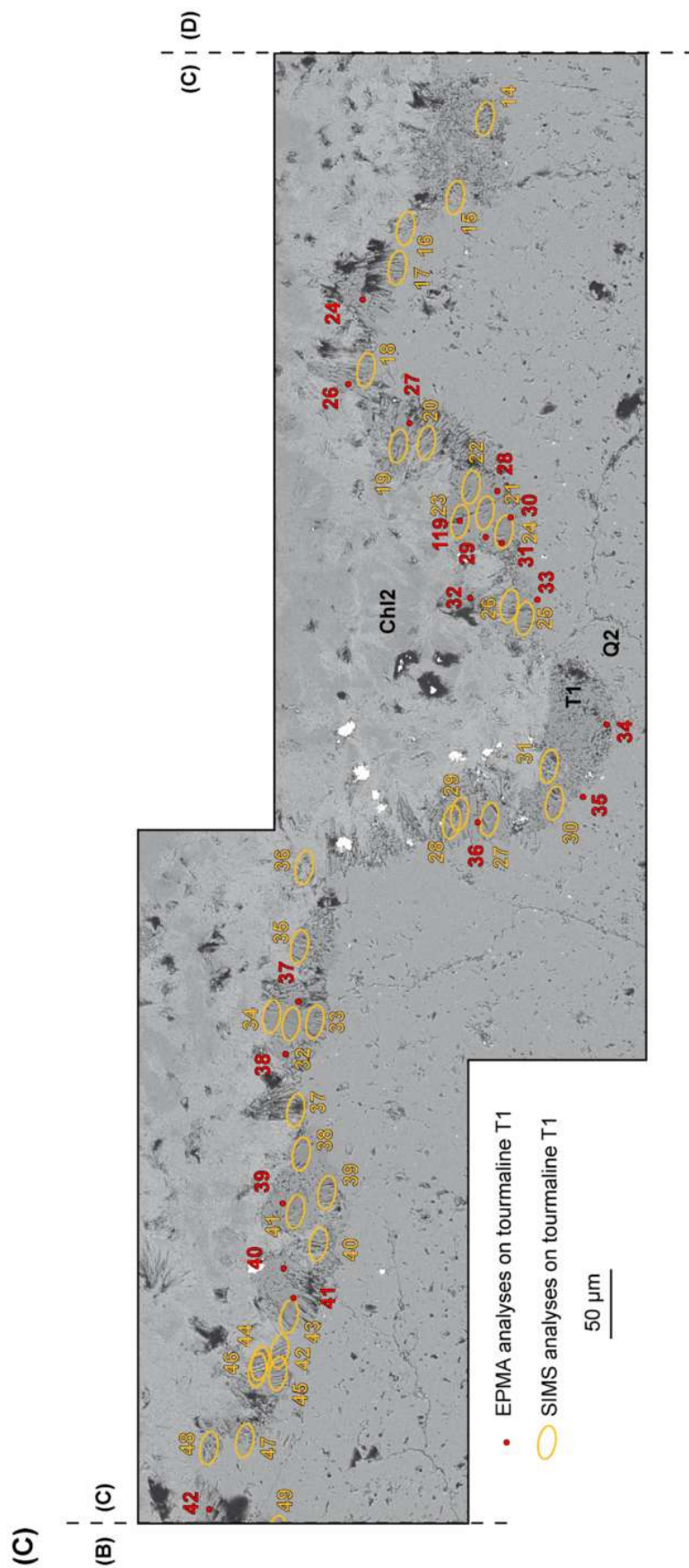
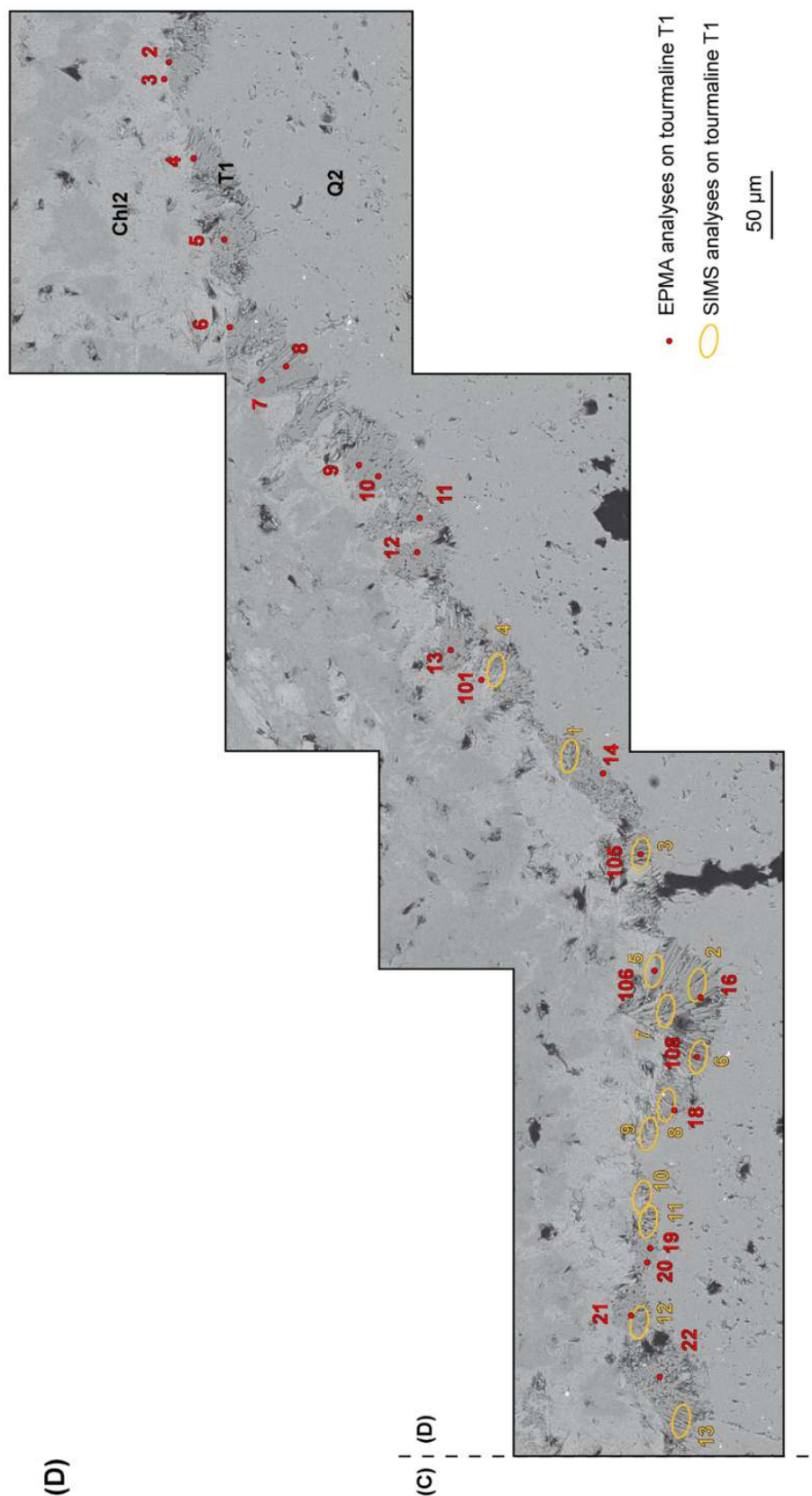


Figure 6. Cont.



**Figure 6.** Locations of the EPMA (red dots for the tourmaline T1 and green dots for the chlorite Chl2) and SIMS (orange ellipse) in situ analyses. (A) BSE map of sample from drillhole S3PD759 402.9 m. The paragenetic assemblage of the pre-ore silicification minerals from the Ranger U deposit (Australia) consists of chlorite Chl2, followed by tourmaline T1 and then by quartz Q2. The insets indicate the location of BSE maps (B–D).

#### 4.1. Scanning Electron Microscopy

Tourmaline and chlorite crystals were characterised using a scanning electron microscope (SEM) Hitachi S-4800 equipped with a SDD-type EDS spectrometer at GeoRessources laboratory (Nancy, France). Backscattered electron (BSE) images were acquired on the polished thin section with an acceleration voltage of 15 kV in order to reveal mineral textures prior to the in situ chemical and isotopic analyses.

#### 4.2. Electron Probe Microanalyses

Electron probe microanalyses (EPMA) were carried out at the GeoRessources laboratory (Nancy, France) prior to the in situ isotopic analyses. Tourmaline and chlorite crystals were analysed using a CAMECA SX100 electron probe micro analyser operating with an emission current of 12 nA, an acceleration voltage of 15 kV and a beam diameter of 1  $\mu\text{m}$ . The following elements, monochromators, standards, and limits of detection were used: Na (TAP, albite, 540 ppm), Si (TAP, albite, 450 ppm), Mg (TAP, olivine, 375 ppm), Al (TAP,  $\text{Al}_2\text{O}_3$ , 350 ppm), K (LPET, orthose, 210 ppm), Ca (PET, andradite, 490 ppm), Ti (LPET,  $\text{MnTiO}_3$ , 290 ppm), Mn (LIF,  $\text{MnTiO}_3$ , 120 ppm) and Fe (LIF,  $\text{Fe}_2\text{O}_3$ , 1650 ppm).

Structural formulae of tourmaline were calculated with the WinTcac software (version 1.03) [48], normalising to 15 cations in T-, Z- and Y-sites, and assuming stoichiometric three atoms for B and four atoms for OH + F, based on the general formula  $\text{XY}_3\text{Z}_6(\text{T}_6\text{O}_{18})(\text{BO}_3)_3\text{V}_3\text{W}$ , where X =  $\text{Na}^+$ ,  $\text{Ca}^{2+}$ ,  $\text{K}^+$ , or vacancy site; Y =  $\text{Fe}^{2+}$ ,  $\text{Mg}^{2+}$ ,  $\text{Mn}^{2+}$ ,  $\text{Al}^{3+}$ ,  $\text{Li}^+$ ,  $\text{Fe}^{3+}$ , or  $\text{Cr}^{3+}$ ; Z =  $\text{Al}^{3+}$ ,  $\text{Fe}^{3+}$ ,  $\text{Ti}^{4+}$ ,  $\text{Mg}^{2+}$ , or  $\text{Cr}^{3+}$ ; T =  $\text{Si}^{4+}$ ,  $\text{Al}^{3+}$ , or  $\text{B}^{3+}$ ; V =  $\text{OH}^-$ ,  $\text{O}^{2-}$  and W =  $\text{OH}^-$ ,  $\text{F}^-$  or  $\text{O}^{2-}$ . The tourmaline nomenclature follows the classification proposed by Henry et al. [49] according to the different solid solution series. Chemical compositions of tourmaline and chlorite are reported in weight per cent oxides (wt.%) and the structural formulae are expressed in atoms per formula unit (*apfu*). The temperature of chlorite formation was calculated using the graphical geothermometer of Bourdelle and Cathelineau [50].

#### 4.3. Secondary Ion Mass Spectrometry

Boron isotopic compositions of tourmaline were measured by secondary ion mass spectrometry (SIMS) at the CRPG-CNRS laboratory (Vandoeuvre-lès-Nancy, France). Isotopic measurements were made using a Cameca IMS 1280-HR instrument by following the analytical procedure described by Chaussidon and Albarède [51]. Analyses were performed on the same polished thin section previously analysed by SEM and EPMA, using a 20 nA beam of primary ions  $\text{O}^-$  accelerated at 13 kV with an ellipsoid ablation spot (20 micron long axis). For each point, a pre-sputtering of 60 s was set in order to clean the surface of contamination. The secondary ions  $^{10}\text{B}^+$  and  $^{11}\text{B}^+$  were accelerated at 10 kV and were measured in monocollection with the axial Faraday cup, during 8 s and 4 s per cycle respectively, over 30 cycles for each measurement. A mass resolution power  $M/\Delta M = 2000$  was sufficient to separate isobaric interferences on the  $^{10}\text{B}^+$  and  $^{11}\text{B}^+$  masses. Instrumental mass fractionation was determined and corrected using three tourmaline reference materials with different chemical compositions: (1) Spivack standard which is a dravite [52], (2) dravite Harvard #108796, and (3) schorl Harvard #112566 [53,54]. The matrix effect was corrected using the dravite Harvard #108796 standard because tourmaline T1 has a composition that is closer to dravite than schorl and its external reproducibility was better than for the Spivack dravite (see below). Each standard was measured several times during the analytical SIMS session following a standard-sample-standard bracketing procedure. The measured isotopic ratios  $^{11}\text{B}/^{10}\text{B}$  were normalised to the NIST SRM 951, whose  $^{11}\text{B}/^{10}\text{B}$  ratio is 4.04362 [55] and expressed in  $\delta^{11}\text{B}$  notation in ‰:

$$\delta^{11}\text{B} = [({}^{11}\text{B}/{}^{10}\text{B})_{\text{sample}}/({}^{11}\text{B}/{}^{10}\text{B})_{\text{SRM 951}}] \times 10^3$$

The external reproducibility ( $2\sigma$ ) on standards is 0.19‰ over 24 analyses for the Spivack dravite, better than 0.13‰ over 28 analyses for the dravite Harvard #108796 and 0.19‰ for 24 analyses for the schorl Harvard #112566. The external error used is that of the relevant reference material, and the total

uncertainty is the quadratic sum of the internal and external errors. The total errors on individual analysis range between 0.3 and 0.6‰.

## 5. Results

### 5.1. Tourmaline Chemistry

The 60 EPMA analyses of hydrothermal tourmaline T1 show relatively homogeneous major element compositions (Table 1) with high Mg (1.9–2.6 *apfu*) and Al (6.3–6.8 *apfu*) contents, and low Fe (0–0.7 *apfu*), Na (0.1–0.2 *apfu*) and Ca (0–0.07 *apfu*) contents, with X-site vacancies of 0.74–0.86 (Figure 7A and Tables 2 and 3). The Ca-Na + K-X-site vacancy ternary diagram showing the X-site occupancy indicates that the tourmaline T1 is alkali-deficient and belongs to the X-vacant group (Figure 7A). The binary diagram showing the  $Fe_{tot}/(Fe_{tot} + Mg)$  versus X-site vacancy/(X-site vacancy + Na + K) ratios highlight the relatively high Mg content of tourmaline T1, corresponding to a Mg-foitite composition (Figure 7B,C). Assuming a stoichiometric content of boron, the average structural formula of tourmaline T1 is  $\square_{0.811}K_{0.012}Na_{0.145}Ca_{0.032}(Mg_{2.272}Fe^{2+}_{0.046}Al_{0.617})Al_6(Si_{6.055}Al_{0.007})(BO_3)_3(OH)_{3.162}$ .

**Table 1.** Chemical composition (wt.%) of tourmaline T1 (EPMA) and calculated H<sub>2</sub>O and B<sub>2</sub>O<sub>3</sub> compositions with the WinTcac software [48].

Analysis #	SiO <sub>2</sub>	TiO <sub>2</sub>	Al <sub>2</sub> O <sub>3</sub>	FeO	MgO	CaO	Na <sub>2</sub> O	K <sub>2</sub> O	F	H <sub>2</sub> O	B <sub>2</sub> O <sub>3</sub>	Total
2	37.93	0.00	35.25	0.35	10.03	0.16	0.53	0.00	0.10	2.97	10.98	98.27
3	38.17	0.00	35.18	0.33	9.55	0.15	0.47	0.00	0.13	2.92	10.91	97.76
4	38.31	0.02	36.10	0.17	9.88	0.16	0.44	0.00	0.02	3.02	11.09	99.21
5	37.02	0.00	34.75	0.26	9.59	0.17	0.36	0.00	0.08	2.87	10.72	95.78
6	38.11	0.00	35.74	0.14	9.78	0.13	0.43	0.04	0.14	2.93	11.00	98.41
7	37.95	0.04	35.96	0.15	9.29	0.18	0.50	0.06	0.12	2.96	10.93	98.09
8	38.38	0.03	35.58	0.18	9.87	0.12	0.47	0.25	0.04	3.04	11.03	98.97
9	37.75	0.00	36.00	0.24	9.47	0.17	0.42	0.00	0.05	2.96	10.95	98.00
10	38.14	0.00	36.01	0.22	9.47	0.16	0.42	0.01	0.12	2.94	11.00	98.44
11	38.59	0.00	35.88	0.23	9.73	0.11	0.43	0.31	0.06	3.04	11.07	99.43
12	38.68	0.02	35.75	0.17	8.22	0.17	0.44	0.00	0.13	2.89	10.80	97.22
13	37.97	0.00	36.28	0.18	9.10	0.22	0.44	0.01	0.06	2.97	10.94	98.15
14	38.61	0.00	34.71	0.24	9.53	0.17	0.49	0.04	0.08	2.96	10.88	97.69
16	37.89	0.00	35.88	0.18	8.79	0.25	0.44	0.06	0.06	2.95	10.83	97.30
18	37.63	0.00	35.06	0.12	9.92	0.15	0.39	0.09	0.09	2.93	10.88	97.24
19	37.25	0.00	34.87	0.17	9.83	0.16	0.48	0.08	0.10	2.93	10.79	96.64
20	37.65	0.00	35.49	0.15	9.60	0.14	0.45	0.16	0.11	2.95	10.88	97.53
21	38.74	0.00	36.00	0.31	9.52	0.14	0.45	0.04	0.06	3.00	11.08	99.33
22	37.09	0.04	35.83	0.23	9.07	0.20	0.37	0.07	0.08	2.91	10.78	96.64
24	37.75	0.02	36.00	0.24	9.66	0.17	0.48	0.09	0.07	3.00	10.99	98.46
26	38.18	0.00	35.58	0.24	9.59	0.16	0.38	0.04	0.12	2.92	10.97	98.16
27	38.81	0.00	35.94	0.29	9.42	0.15	0.39	0.22	0.07	3.01	11.06	99.34
28	36.70	0.01	34.70	0.11	9.88	0.14	0.49	0.00	0.05	2.92	10.71	95.70
29	37.37	0.03	35.33	0.23	9.63	0.23	0.48	0.00	0.09	2.95	10.84	97.15
30	36.07	0.00	33.94	0.25	10.17	0.12	0.50	0.09	0.00	2.94	10.60	94.68
31	38.35	0.00	35.88	0.20	9.76	0.20	0.45	0.06	0.07	3.00	11.05	99.00
32	37.57	0.00	35.99	0.27	9.23	0.29	0.45	0.05	0.13	2.94	10.89	97.77
33	38.31	0.01	35.63	0.22	9.62	0.09	0.42	0.10	0.04	2.98	10.99	98.40
34	37.10	0.00	35.04	0.08	9.78	0.14	0.45	0.03	0.02	2.95	10.78	96.37
35	37.60	0.01	34.94	0.07	9.93	0.09	0.46	0.12	0.10	2.93	10.85	97.08
36	36.05	0.02	33.63	0.17	10.28	0.12	0.55	0.06	0.13	2.88	10.56	94.41
37	37.85	0.00	35.46	0.17	9.64	0.15	0.49	0.02	0.10	2.95	10.91	97.73
38	38.30	0.00	34.81	0.51	9.84	0.18	0.55	0.06	0.03	3.02	10.94	98.23
39	37.18	0.01	35.09	0.31	9.58	0.23	0.43	0.03	0.13	2.90	10.79	96.64
40	37.74	0.08	35.47	0.30	9.73	0.21	0.39	0.04	0.11	2.94	10.94	97.92

Table 1. Cont.

Analysis #	SiO <sub>2</sub>	TiO <sub>2</sub>	Al <sub>2</sub> O <sub>3</sub>	FeO	MgO	CaO	Na <sub>2</sub> O	K <sub>2</sub> O	F	H <sub>2</sub> O	B <sub>2</sub> O <sub>3</sub>	Total
41	37.71	0.00	34.95	0.27	9.29	0.21	0.45	0.01	0.06	2.93	10.77	96.62
42	38.06	0.00	35.72	0.35	9.79	0.17	0.47	0.27	0.07	3.03	11.02	98.94
43	37.85	0.04	34.64	0.38	9.87	0.15	0.61	0.04	0.02	3.01	10.86	97.47
44	35.53	0.06	32.51	0.32	9.53	0.12	0.58	0.04	0.12	2.79	10.24	91.80
45	37.54	0.05	34.94	0.05	9.89	0.14	0.48	0.04	0.02	2.97	10.84	96.97
46	38.16	0.04	34.24	0.21	9.75	0.12	0.65	0.18	0.06	3.01	10.81	97.21
47	38.52	0.01	35.89	0.10	9.43	0.15	0.44	0.00	0.06	2.97	11.01	98.57
48	36.61	0.07	34.43	0.14	10.90	0.15	0.54	0.00	0.10	2.97	10.85	96.73
49	37.40	0.00	34.48	0.35	9.63	0.21	0.50	0.08	0.10	2.93	10.74	96.37
101	36.56	0.01	32.88	4.97	8.83	0.33	0.42	0.12	0.00	3.01	10.74	97.97
105	37.89	0.00	35.21	0.16	9.41	0.20	0.39	0.01	0.00	2.95	10.84	97.06
106	39.35	0.02	36.63	0.22	9.66	0.22	0.49	0.02	0.00	3.09	11.25	100.96
108	38.57	0.00	35.01	0.23	9.39	0.28	0.47	0.05	0.00	3.01	10.89	97.90
119	35.64	0.02	33.63	0.28	8.56	0.22	0.40	0.03	0.00	2.81	10.24	91.96
134	40.00	0.00	36.71	0.16	10.01	0.14	0.55	0.01	0.00	3.13	11.39	102.12
139	37.90	0.02	33.24	0.45	8.92	0.16	0.67	0.09	0.00	2.96	10.52	94.93
140	37.75	0.01	33.71	0.18	8.67	0.29	0.38	0.09	0.00	2.89	10.49	94.46
141	36.29	0.02	33.27	1.73	9.78	0.25	0.45	0.04	0.00	2.94	10.61	95.38
144	39.66	0.00	35.53	0.47	8.86	0.27	0.49	0.07	0.00	3.05	11.03	99.46
145	38.57	0.00	34.24	0.39	9.22	0.39	0.46	0.03	0.00	2.99	10.78	97.07
146	38.07	0.00	34.58	0.26	9.61	0.22	0.47	0.02	0.00	2.98	10.82	97.04
148	39.31	0.02	35.80	0.43	8.17	0.32	0.52	0.07	0.00	3.04	10.90	98.57
150	37.01	0.02	34.69	0.20	9.27	0.20	0.41	0.04	0.00	2.91	10.65	95.40
151	36.56	0.00	33.36	0.28	8.66	0.17	0.38	0.02	0.00	2.81	10.32	92.59
152	39.16	0.01	35.95	0.41	9.82	0.18	0.52	0.06	0.00	3.09	11.18	100.38

Table 2. Structural formula of tourmaline T1 (T, Z and Y sites) calculated with the WinTcac software [48].

Analysis #	Si(T)	B(T)	Al(T)	Total (T)	Al(Z)	Total (Z)	Al(Y)	Ti(Y)	Fe <sup>2+</sup> (Y)	Mn <sup>2+</sup> (Y)	Mg(Y)	Total (Y)
2	6.01	0.00	0.00	6.01	6.00	6.00	0.58	0.00	0.05	0.00	2.37	2.99
3	6.08	0.00	0.00	6.08	6.00	6.00	0.61	0.00	0.04	0.00	2.27	2.92
4	6.00	0.00	0.00	6.00	6.00	6.00	0.67	0.00	0.02	0.00	2.31	3.00
5	6.00	0.00	0.00	6.00	6.00	6.00	0.64	0.00	0.04	0.00	2.32	3.00
6	6.02	0.00	0.00	6.02	6.00	6.00	0.66	0.00	0.02	0.00	2.30	2.98
7	6.03	0.00	0.00	6.03	6.00	6.00	0.74	0.01	0.02	0.00	2.20	2.97
8	6.05	0.00	0.00	6.05	6.00	6.00	0.61	0.00	0.02	0.00	2.32	2.95
9	5.99	0.01	0.00	6.00	6.00	6.00	0.73	0.00	0.03	0.00	2.24	3.01
10	6.03	0.00	0.00	6.03	6.00	6.00	0.71	0.00	0.03	0.00	2.23	2.97
11	6.06	0.00	0.00	6.06	6.00	6.00	0.64	0.00	0.03	0.00	2.28	2.94
12	6.22	0.00	0.00	6.22	6.00	6.00	0.78	0.00	0.02	0.00	1.97	2.78
13	6.03	0.00	0.00	6.03	6.00	6.00	0.79	0.00	0.02	0.00	2.16	2.97
14	6.17	0.00	0.00	6.17	6.00	6.00	0.53	0.00	0.03	0.00	2.27	2.84
16	6.08	0.00	0.00	6.08	6.00	6.00	0.79	0.00	0.02	0.00	2.10	2.92
18	6.01	0.00	0.00	6.01	6.00	6.00	0.60	0.00	0.02	0.00	2.36	2.99
19	6.00	0.01	0.00	6.01	6.00	6.00	0.62	0.00	0.02	0.00	2.36	3.00
20	6.01	0.00	0.00	6.01	6.00	6.00	0.68	0.00	0.02	0.00	2.29	2.99
21	6.08	0.00	0.00	6.08	6.00	6.00	0.66	0.00	0.04	0.00	2.23	2.92
22	5.98	0.00	0.02	6.00	6.00	6.00	0.79	0.01	0.03	0.00	2.18	3.00
24	5.97	0.01	0.02	6.00	6.00	6.00	0.69	0.00	0.03	0.00	2.28	3.01
26	6.05	0.00	0.00	6.05	6.00	6.00	0.65	0.00	0.03	0.00	2.27	2.95
27	6.10	0.00	0.00	6.10	6.00	6.00	0.66	0.00	0.04	0.00	2.21	2.90
28	5.96	0.01	0.03	6.00	6.00	6.00	0.61	0.00	0.02	0.00	2.39	3.01
29	5.99	0.01	0.01	6.00	6.00	6.00	0.67	0.00	0.03	0.00	2.30	3.01
30	5.92	0.02	0.06	6.00	6.00	6.00	0.50	0.00	0.03	0.00	2.49	3.02
31	6.03	0.00	0.00	6.03	6.00	6.00	0.65	0.00	0.03	0.00	2.29	2.97
32	6.00	0.00	0.00	6.00	6.00	6.00	0.77	0.00	0.04	0.00	2.20	3.00
33	6.06	0.00	0.00	6.06	6.00	6.00	0.64	0.00	0.03	0.00	2.27	2.94
34	5.98	0.01	0.01	6.00	6.00	6.00	0.65	0.00	0.01	0.00	2.35	3.01
35	6.02	0.00	0.00	6.02	6.00	6.00	0.60	0.00	0.01	0.00	2.37	2.98

Table 2. Cont.

Analysis #	Si(T)	B(T)	Al(T)	Total (T)	Al(Z)	Total (Z)	Al(Y)	Ti(Y)	Fe <sup>2+</sup> (Y)	Mn <sup>2+</sup> (Y)	Mg(Y)	Total (Y)
36	5.93	0.02	0.05	6.00	6.00	6.00	0.47	0.00	0.02	0.00	2.52	3.02
37	6.03	0.00	0.00	6.03	6.00	6.00	0.66	0.00	0.02	0.00	2.29	2.97
38	6.08	0.00	0.00	6.08	6.00	6.00	0.52	0.00	0.07	0.00	2.33	2.92
39	5.99	0.01	0.00	6.00	6.00	6.00	0.66	0.00	0.04	0.00	2.30	3.01
40	6.00	0.01	0.00	6.01	6.00	6.00	0.64	0.01	0.04	0.00	2.31	3.00
41	6.08	0.00	0.00	6.08	6.00	6.00	0.65	0.00	0.04	0.00	2.23	2.92
42	6.01	0.00	0.00	6.01	6.00	6.00	0.64	0.00	0.05	0.00	2.30	2.99
43	6.06	0.00	0.00	6.06	6.00	6.00	0.53	0.01	0.05	0.00	2.35	2.94
44	6.03	0.00	0.00	6.03	6.00	6.00	0.50	0.01	0.05	0.00	2.41	2.97
45	6.02	0.00	0.00	6.02	6.00	6.00	0.60	0.01	0.01	0.00	2.36	2.98
46	6.14	0.00	0.00	6.14	6.00	6.00	0.49	0.01	0.03	0.00	2.34	2.86
47	6.08	0.00	0.00	6.08	6.00	6.00	0.68	0.00	0.01	0.00	2.22	2.92
48	5.87	0.03	0.11	6.00	6.00	6.00	0.39	0.01	0.02	0.00	2.60	3.03
49	6.05	0.00	0.00	6.05	6.00	6.00	0.58	0.00	0.05	0.00	2.32	2.95
101	5.91	0.03	0.05	6.00	6.00	6.00	0.22	0.00	0.67	0.01	2.13	3.03
105	6.08	0.00	0.00	6.08	6.00	6.00	0.65	0.00	0.02	0.00	2.25	2.93
106	6.08	0.00	0.00	6.08	6.00	6.00	0.67	0.00	0.03	0.00	2.22	2.92
108	6.15	0.00	0.00	6.15	6.00	6.00	0.58	0.00	0.03	0.00	2.23	2.85
119	6.05	0.00	0.00	6.05	6.00	6.00	0.73	0.00	0.04	0.02	2.17	2.95
134	6.10	0.00	0.00	6.10	6.00	6.00	0.60	0.00	0.02	0.00	2.28	2.90
139	6.26	0.00	0.00	6.26	6.00	6.00	0.47	0.00	0.06	0.00	2.20	2.74
140	6.25	0.00	0.00	6.25	6.00	6.00	0.58	0.00	0.03	0.00	2.14	2.75
141	5.95	0.02	0.03	6.00	6.00	6.00	0.39	0.00	0.24	0.00	2.39	3.02
144	6.25	0.00	0.00	6.25	6.00	6.00	0.60	0.00	0.06	0.00	2.08	2.75
145	6.22	0.00	0.00	6.22	6.00	6.00	0.51	0.00	0.05	0.00	2.22	2.78
146	6.12	0.00	0.00	6.12	6.00	6.00	0.55	0.00	0.04	0.00	2.30	2.88
148	6.27	0.00	0.00	6.27	6.00	6.00	0.73	0.00	0.06	0.00	1.94	2.73
150	6.04	0.00	0.00	6.04	6.00	6.00	0.67	0.00	0.03	0.00	2.26	2.96
151	6.16	0.00	0.00	6.16	6.00	6.00	0.62	0.00	0.04	0.00	2.18	2.84
152	6.09	0.00	0.00	6.09	6.00	6.00	0.59	0.00	0.05	0.00	2.28	2.91

Table 3. Structural formula of tourmaline T1 (X, V and W sites) calculated with the WinTcac software [48].

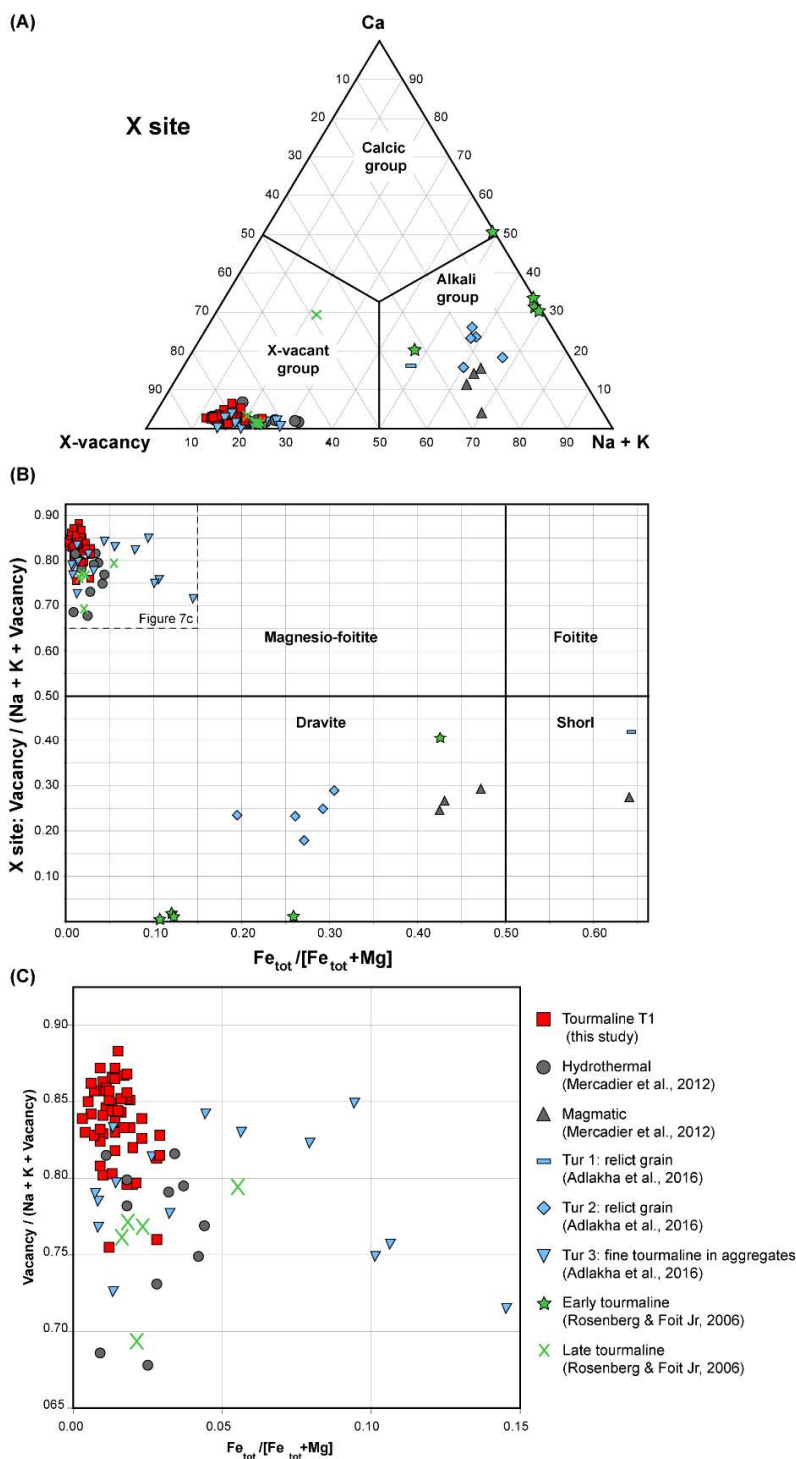
Analysis #	Ca(X)	Na(X)	K(X)	vacancy(X)	Total(X)	OH(V)	OH(W)	F(W)	O(W)	Total(V+W)
2	0.03	0.16	0.00	0.81	1.00	3.00	0.14	0.05	0.81	4.00
3	0.03	0.15	0.00	0.83	1.00	3.00	0.11	0.07	0.83	4.00
4	0.03	0.13	0.00	0.84	1.00	3.00	0.15	0.01	0.84	4.00
5	0.03	0.11	0.00	0.86	1.00	3.00	0.10	0.04	0.86	4.00
6	0.02	0.13	0.01	0.84	1.00	3.00	0.09	0.07	0.84	4.00
7	0.03	0.15	0.01	0.80	1.00	3.00	0.14	0.06	0.80	4.00
8	0.02	0.14	0.05	0.79	1.00	3.00	0.19	0.02	0.79	4.00
9	0.03	0.13	0.00	0.84	1.00	3.00	0.14	0.03	0.84	4.00
10	0.03	0.13	0.00	0.84	1.00	3.00	0.10	0.06	0.84	4.00
11	0.02	0.13	0.06	0.79	1.00	3.00	0.18	0.03	0.79	4.00
12	0.03	0.14	0.00	0.83	1.00	3.00	0.10	0.07	0.83	4.00
13	0.04	0.14	0.00	0.83	1.00	3.00	0.15	0.03	0.83	4.00
14	0.03	0.15	0.01	0.81	1.00	3.00	0.15	0.04	0.81	4.00
16	0.04	0.14	0.01	0.81	1.00	3.00	0.16	0.03	0.81	4.00
18	0.03	0.12	0.02	0.84	1.00	3.00	0.12	0.05	0.84	4.00
19	0.03	0.15	0.02	0.81	1.00	3.00	0.15	0.05	0.80	4.00
20	0.02	0.14	0.03	0.80	1.00	3.00	0.14	0.06	0.80	4.00
21	0.02	0.14	0.01	0.83	1.00	3.00	0.14	0.03	0.83	4.00
22	0.04	0.12	0.01	0.84	1.00	3.00	0.13	0.04	0.83	4.00
24	0.03	0.15	0.02	0.81	1.00	3.00	0.17	0.04	0.80	4.00
26	0.03	0.12	0.01	0.85	1.00	3.00	0.09	0.06	0.85	4.00
27	0.03	0.12	0.04	0.81	1.00	3.00	0.15	0.04	0.81	4.00
28	0.02	0.15	0.00	0.82	1.00	3.00	0.17	0.03	0.81	4.00
29	0.04	0.15	0.00	0.81	1.00	3.00	0.15	0.05	0.81	4.00
30	0.02	0.16	0.02	0.80	1.00	3.00	0.22	0.00	0.78	4.00

Table 3. Cont.

Analysis #	Ca(X)	Na(X)	K(X)	vacancy(X)	Total(X)	OH(V)	OH(W)	F(W)	O(W)	Total(V+W)
31	0.03	0.14	0.01	0.82	1.00	3.00	0.15	0.04	0.82	4.00
32	0.05	0.14	0.01	0.80	1.00	3.00	0.13	0.07	0.80	4.00
33	0.02	0.13	0.02	0.84	1.00	3.00	0.14	0.02	0.84	4.00
34	0.02	0.14	0.01	0.83	1.00	3.00	0.17	0.01	0.82	4.00
35	0.02	0.14	0.03	0.82	1.00	3.00	0.13	0.05	0.82	4.00
36	0.02	0.18	0.01	0.79	1.00	3.00	0.16	0.07	0.77	4.00
37	0.03	0.15	0.00	0.82	1.00	3.00	0.13	0.05	0.82	4.00
38	0.03	0.17	0.01	0.79	1.00	3.00	0.20	0.02	0.79	4.00
39	0.04	0.13	0.01	0.82	1.00	3.00	0.12	0.07	0.81	4.00
40	0.04	0.12	0.01	0.84	1.00	3.00	0.12	0.06	0.83	4.00
41	0.04	0.14	0.00	0.82	1.00	3.00	0.15	0.03	0.82	4.00
42	0.03	0.14	0.05	0.77	1.00	3.00	0.19	0.04	0.77	4.00
43	0.03	0.19	0.01	0.78	1.00	3.00	0.21	0.01	0.78	4.00
44	0.02	0.19	0.01	0.78	1.00	3.00	0.16	0.06	0.78	4.00
45	0.02	0.15	0.01	0.82	1.00	3.00	0.17	0.01	0.82	4.00
46	0.02	0.20	0.04	0.74	1.00	3.00	0.23	0.03	0.74	4.00
47	0.03	0.14	0.00	0.84	1.00	3.00	0.13	0.03	0.84	4.00
48	0.03	0.17	0.00	0.81	1.00	3.00	0.17	0.05	0.78	4.00
49	0.04	0.16	0.02	0.79	1.00	3.00	0.16	0.05	0.79	4.00
101	0.06	0.13	0.03	0.79	1.00	3.00	0.25	0.00	0.75	4.00
105	0.03	0.12	0.00	0.84	1.00	3.00	0.16	0.00	0.84	4.00
106	0.04	0.15	0.00	0.81	1.00	3.00	0.19	0.00	0.81	4.00
108	0.05	0.15	0.01	0.80	1.00	3.00	0.20	0.00	0.80	4.00
119	0.04	0.13	0.01	0.82	1.00	3.00	0.18	0.00	0.82	4.00
134	0.02	0.16	0.00	0.81	1.00	3.00	0.19	0.00	0.81	4.00
139	0.03	0.22	0.02	0.74	1.00	3.00	0.26	0.00	0.74	4.00
140	0.05	0.12	0.02	0.81	1.00	3.00	0.19	0.00	0.81	4.00
141	0.04	0.14	0.01	0.81	1.00	3.00	0.22	0.00	0.78	4.00
144	0.05	0.15	0.01	0.79	1.00	3.00	0.21	0.00	0.79	4.00
145	0.07	0.14	0.01	0.78	1.00	3.00	0.22	0.00	0.78	4.00
146	0.04	0.15	0.00	0.81	1.00	3.00	0.19	0.00	0.81	4.00
148	0.06	0.16	0.01	0.77	1.00	3.00	0.23	0.00	0.77	4.00
150	0.04	0.13	0.01	0.83	1.00	3.00	0.17	0.00	0.83	4.00
151	0.03	0.12	0.00	0.84	1.00	3.00	0.16	0.00	0.84	4.00
152	0.03	0.16	0.01	0.80	1.00	3.00	0.20	0.00	0.80	4.00

### 5.2. Chlorite Chemistry and Thermometry

A total of 14 EPMA analyses were obtained on hydrothermal chlorite Chl2 and 16 EPMA analyses on retrometamorphic chlorite Chl1 for comparison. Analyses were carried out on >5  $\mu\text{m}$  size chlorite grains. The chlorite Chl1 is a Fe-Mg chlorite with high Fe contents (2.93–3.40 *apfu*) and relatively low Mg contents (1.10–1.49 *apfu*), with Si/Al = 1.04–1.16, and Mg/(Mg + Fe<sub>tot</sub>) = 0.25–0.33 (Tables 4 and 5). The chlorite Chl2 corresponds to Mg-chlorite with compositions that lie between the clinochlore and Mg-amesite fields (Figure 8A). It has relatively low Fe contents (0.28–0.83 *apfu*) and high Mg contents (3.08–3.84 *apfu*), with Si/Al = 1.08–1.22, and Mg/(Mg + Fe<sub>tot</sub>) = 0.80–0.93 consistent with other Mg-chlorite Chl2 (Mg/(Mg + Fe<sub>tot</sub>) = 0.89–0.92) observed elsewhere in the deposit [4]. All Fe is assumed to be ferrous in the calculations of the structural formulae.



**Figure 7.** Classification of tourmaline T1 at the Ranger U deposit (Australia) and for different generations of tourmaline in other unconformity-related U deposits from the Athabasca Basin (Canada [31,33,56]) [48]. (A) Ca-Na + K-X-site vacancy ternary diagram showing the X-site occupancy; (B) binary diagram showing the  $Fe_{tot}/(Fe_{tot} + Mg)$  versus X-site vacancy/(X-site vacancy + Na + K) ratios; (C) zoom on the Mg-foitite domain on the  $Fe_{tot}/(Fe_{tot} + Mg)$  versus X-site vacancy/(X-site vacancy + Na + K) diagram. For Canadian deposits, “Hydrothermal” (Mercadier et al. [33]), “Tur 3” (Adlakha et al. [31]) and “Late tourmaline” (Rosenberg and Foit Jr, [56]) correspond to Mg-foitite. Note that each point for “Hydrothermal”, Magmatic” (Mercadier et al. [33]), “Tur1”, “Tur2”, “Tur3” (Adlakha et al. [31]), “early” and “late tourmaline” (Rosenberg and Foit Jr [56]) compositions correspond to the mean values for each sample or generation.

**Table 4.** Chemical composition (wt.%) and calculated temperature [50] of chlorite Chl1 and Chl2 (EPMA).

Analysis #	Na <sub>2</sub> O	MgO	Al <sub>2</sub> O <sub>3</sub>	SiO <sub>2</sub>	K <sub>2</sub> O	CaO	MnO	FeO	TiO <sub>2</sub>	Total	Calculated T (°C)
Chl1 2	0.06	6.94	21.66	27.54	0.81	0.09	0.13	33.10	0.03	90.36	162
Chl1 3	0.08	7.26	20.71	27.18	0.60	0.13	0.19	32.83	0.04	89.03	169
Chl1 4	0.00	7.97	20.77	26.84	0.44	0.11	0.04	32.55	0.04	88.76	182
Chl1 6	0.04	7.23	20.82	26.40	0.36	0.07	0.02	35.16	0.04	90.12	216
Chl1 8	0.00	7.92	19.53	25.95	0.19	0.09	0.14	34.35	0.03	88.19	240
Chl1 13	0.03	9.11	19.03	25.95	0.06	0.12	0.07	33.44	0.02	87.83	279
Chl1 20	0.02	6.71	19.39	25.76	0.02	0.04	0.04	36.79	0.05	88.80	248
Chl1 21	0.00	7.59	19.29	25.11	0.04	0.03	0.07	35.28	0.04	87.45	298
Chl1 22	0.05	8.27	19.15	25.51	0.04	0.07	0.07	33.37	0.10	86.64	246
Chl1 33	0.00	6.93	20.86	25.68	0.05	0.02	0.05	35.29	0.01	88.87	224
Chl1 38	0.04	6.95	20.36	25.08	0.05	0.08	0.16	36.79	0.01	89.51	332
Chl1 39	0.02	7.12	20.17	25.26	0.50	0.11	0.09	33.18	0.03	86.47	221
Chl1 44	0.05	6.88	21.30	26.94	0.60	0.13	0.23	32.79	0.03	88.96	167
Chl1 45	0.00	8.31	20.01	25.84	0.07	0.02	0.01	33.82	0.14	88.21	235
Chl1 46	0.01	7.89	20.22	25.78	0.35	0.03	0.07	33.46	0.08	87.89	227
Chl1 52	0.03	7.31	19.70	24.80	0.11	0.11	0.07	35.30	0.09	87.53	312
Chl2 153	0.02	21.76	25.30	32.56	0.01	0.11	0.05	6.16	0.02	86.00	101
Chl2 154	0.00	23.40	25.33	32.31	0.03	0.08	0.00	4.54	0.02	85.71	109
Chl2 155	0.02	26.82	23.40	31.83	0.03	0.01	0.00	3.58	0.00	85.68	136
Chl2 156	0.04	25.31	21.04	30.25	0.02	0.13	0.00	6.99	0.00	83.78	163
Chl2 157	0.03	22.99	21.62	30.25	0.00	0.05	0.03	10.03	0.00	85.01	153
Chl2 158	0.00	23.96	24.48	31.26	0.07	0.05	0.08	5.70	0.04	85.64	129
Chl2 159	0.03	23.77	24.66	31.81	0.06	0.05	0.13	4.80	0.00	85.29	117
Chl2 160	0.02	25.14	24.39	31.65	0.02	0.03	0.01	3.88	0.00	85.15	125
Chl2 161	0.00	23.82	24.68	31.42	0.04	0.06	0.00	4.52	0.00	84.53	119
Chl2 162	0.02	24.97	23.95	31.47	0.05	0.05	0.00	3.85	0.00	84.36	124
Chl2 163	0.00	24.02	23.69	31.45	0.03	0.05	0.00	4.79	0.01	84.06	119
Chl2164	0.03	26.40	22.02	30.72	0.04	0.07	0.00	4.45	0.00	83.73	151
Chl2 165	0.00	25.71	23.87	31.40	0.06	0.06	0.00	3.97	0.00	85.06	133
Chl2 166	0.00	22.65	24.18	30.87	0.04	0.05	0.05	5.87	0.00	83.73	119

**Table 5.** Structural formula and occupancy sites for chlorite Chl1 and Chl2 calculated on a basis of 14 oxygens.

Analysis #	Na ( <i>apfu</i> )	Mg ( <i>apfu</i> )	Al tot ( <i>apfu</i> )	Al IV ( <i>apfu</i> )	Al VI ( <i>apfu</i> )	Si ( <i>apfu</i> )	K ( <i>apfu</i> )	Ca ( <i>apfu</i> )	Mn ( <i>apfu</i> )	Fe ( <i>apfu</i> )	Ti ( <i>apfu</i> )
Chl1 2	0.01	1.10	2.70	1.08	1.62	2.92	0.11	0.01	0.01	2.93	0.00
Chl1 3	0.02	1.16	2.63	1.07	1.55	2.93	0.08	0.02	0.02	2.96	0.00
Chl1 4	0.00	1.28	2.64	1.11	1.53	2.89	0.06	0.01	0.00	2.93	0.00
Chl1 6	0.01	1.16	2.64	1.16	1.48	2.84	0.05	0.01	0.00	3.16	0.00
Chl1 8	0.00	1.30	2.53	1.15	1.38	2.85	0.03	0.01	0.01	3.16	0.00
Chl1 13	0.01	1.49	2.46	1.15	1.32	2.85	0.01	0.01	0.01	3.07	0.00
Chl1 20	0.00	1.11	2.52	1.15	1.37	2.85	0.00	0.00	0.00	3.40	0.00
Chl1 21	0.00	1.26	2.54	1.20	1.34	2.80	0.01	0.00	0.01	3.30	0.00
Chl1 22	0.01	1.37	2.52	1.15	1.36	2.85	0.01	0.01	0.01	3.11	0.01
Chl1 33	0.00	1.13	2.69	1.19	1.49	2.81	0.01	0.00	0.00	3.22	0.00
Chl1 38	0.01	1.14	2.63	1.25	1.39	2.75	0.01	0.01	0.01	3.38	0.00
Chl1 39	0.00	1.19	2.66	1.17	1.49	2.83	0.07	0.01	0.01	3.11	0.00
Chl1 44	0.01	1.10	2.70	1.10	1.60	2.90	0.08	0.01	0.02	2.95	0.00
Chl1 45	0.00	1.35	2.58	1.17	1.41	2.83	0.01	0.00	0.00	3.09	0.01
Chl1 46	0.00	1.29	2.62	1.17	1.45	2.83	0.05	0.00	0.01	3.07	0.01
Chl1 52	0.01	1.22	2.59	1.23	1.37	2.77	0.02	0.01	0.01	3.30	0.01
Chl2 153	0.00	3.08	2.83	0.91	1.91	3.09	0.00	0.01	0.00	0.49	0.00
Chl2 154	0.00	3.30	2.82	0.95	1.87	3.05	0.00	0.01	0.00	0.36	0.00
Chl2 155	0.00	3.78	2.61	0.99	1.62	3.01	0.00	0.00	0.00	0.28	0.00
Chl2 156	0.01	3.73	2.45	1.01	1.45	2.99	0.00	0.01	0.00	0.58	0.00
Chl2 157	0.01	3.39	2.52	1.01	1.51	2.99	0.00	0.01	0.00	0.83	0.00
Chl2 158	0.00	3.41	2.76	1.01	1.74	2.99	0.01	0.01	0.01	0.46	0.00
Chl2 159	0.01	3.38	2.77	0.97	1.80	3.03	0.01	0.01	0.01	0.38	0.00
Chl2 160	0.00	3.56	2.73	0.99	1.74	3.01	0.00	0.00	0.00	0.31	0.00
Chl2 161	0.00	3.41	2.79	0.98	1.81	3.02	0.00	0.01	0.00	0.36	0.00
Chl2 162	0.00	3.57	2.71	0.98	1.73	3.02	0.01	0.01	0.00	0.31	0.00
Chl2 163	0.00	3.46	2.70	0.96	1.74	3.04	0.00	0.01	0.00	0.39	0.00
Chl2164	0.01	3.84	2.53	1.00	1.53	3.00	0.00	0.01	0.00	0.36	0.00
Chl2 165	0.00	3.66	2.68	1.00	1.68	3.00	0.01	0.01	0.00	0.32	0.00
Chl2 166	0.00	3.30	2.78	0.98	1.80	3.02	0.00	0.01	0.00	0.48	0.00

The geothermometer of Bourdelle and Cathelineau [50] assumes that quartz and water activities are equal to 1 and is valid for a temperature range of 50 to 350 °C, which makes it applicable to our data based on temperatures estimated from the previously mentioned fluid inclusion studies [10,30,46,47]. This thermometer requires chlorite-quartz equilibrium, and produces estimates of the crystallization temperatures of retrometamorphic chlorite Ch1 between 162 and 332 °C (average ± standard deviation values are 235 ± 50) and diagenetic-hydrothermal chlorite Ch2 between 101 and 163 °C (average ± standard deviation values are 128 ± 28) when plotted in the Si-R<sup>2+</sup> diagram of Wiewióra and Weiss (Figure 8B [57]).

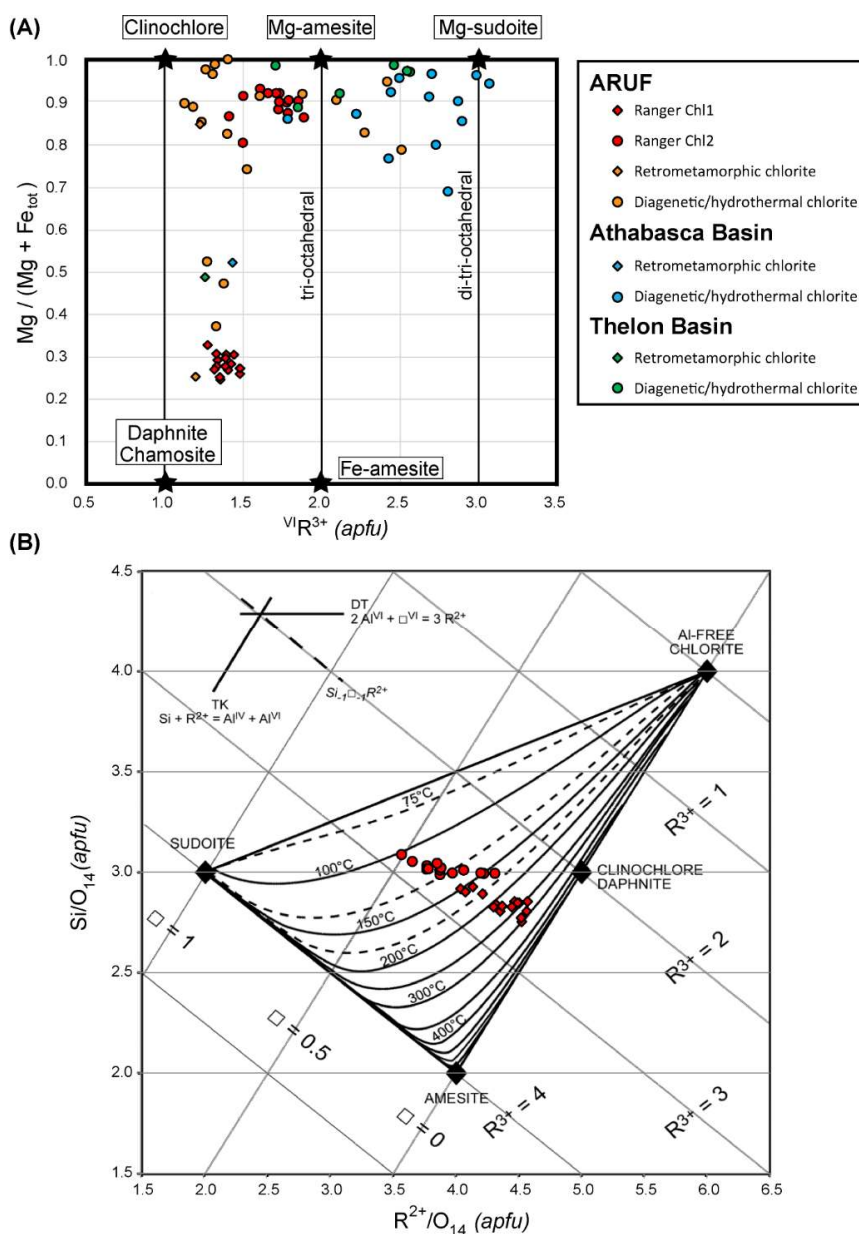


**Figure 8.** (A) Classification diagram of Plissart et al. [58] for tri- and di-trioctahedral chlorite. Compositions of chlorite Ch1 and Ch2 from Ranger deposit (this study) are plotted together with chlorite from other deposits from the ARUF [30,46,59], the Athabasca Basin [11,60,61] and the Thelon Basin [19] for comparison. For data from the ARUF (except for Ranger, this study) and the Canadian basins, the plotted data corresponds to the mean compositions for each sample or generation. (B) Distribution of temperatures for chlorite Ch1 and Ch2 from Ranger deposit (this study) determined by chlorite thermometry plotted in a T-R<sup>2+</sup>-Si diagram, with R<sup>2+</sup> = Mm + Mn + Fe (apfu) [57].

### 5.3. Boron Isotopes in Tourmaline

Due to the large spot size compared to the tourmaline T1 needles width, SIMS analyses are occurring across many different needles leading to a homogenisation of the  $\delta^{11}\text{B}$  values. The tourmaline T1 displays a range of positive  $\delta^{11}\text{B}$  values (0.6–9.4‰,  $n = 76$ , Table 6 and Figure 9). The distribution of  $\delta^{11}\text{B}$  values shows a unique mode at  $\sim 4.3\text{‰}$  (average =  $3.7 \pm 1.8\text{‰}$  ( $1\sigma$ ) and median =  $3.4\text{‰}$ ). There is no relationship between  $\delta^{11}\text{B}$  value and analytical spot location along the investigated tourmaline T1 fringe, or within a single T1 rosette. Therefore, even though some homogenisation of the data may have occurred due to the large spot size compared to the tourmaline needles size, there is no obvious systematic variation of  $\delta^{11}\text{B}$  value along the c-axis. Moreover, there is no visible relationship between  $\delta^{11}\text{B}$  value and the chemical composition of tourmaline as measured by EPMA since both parameters are relatively constant.

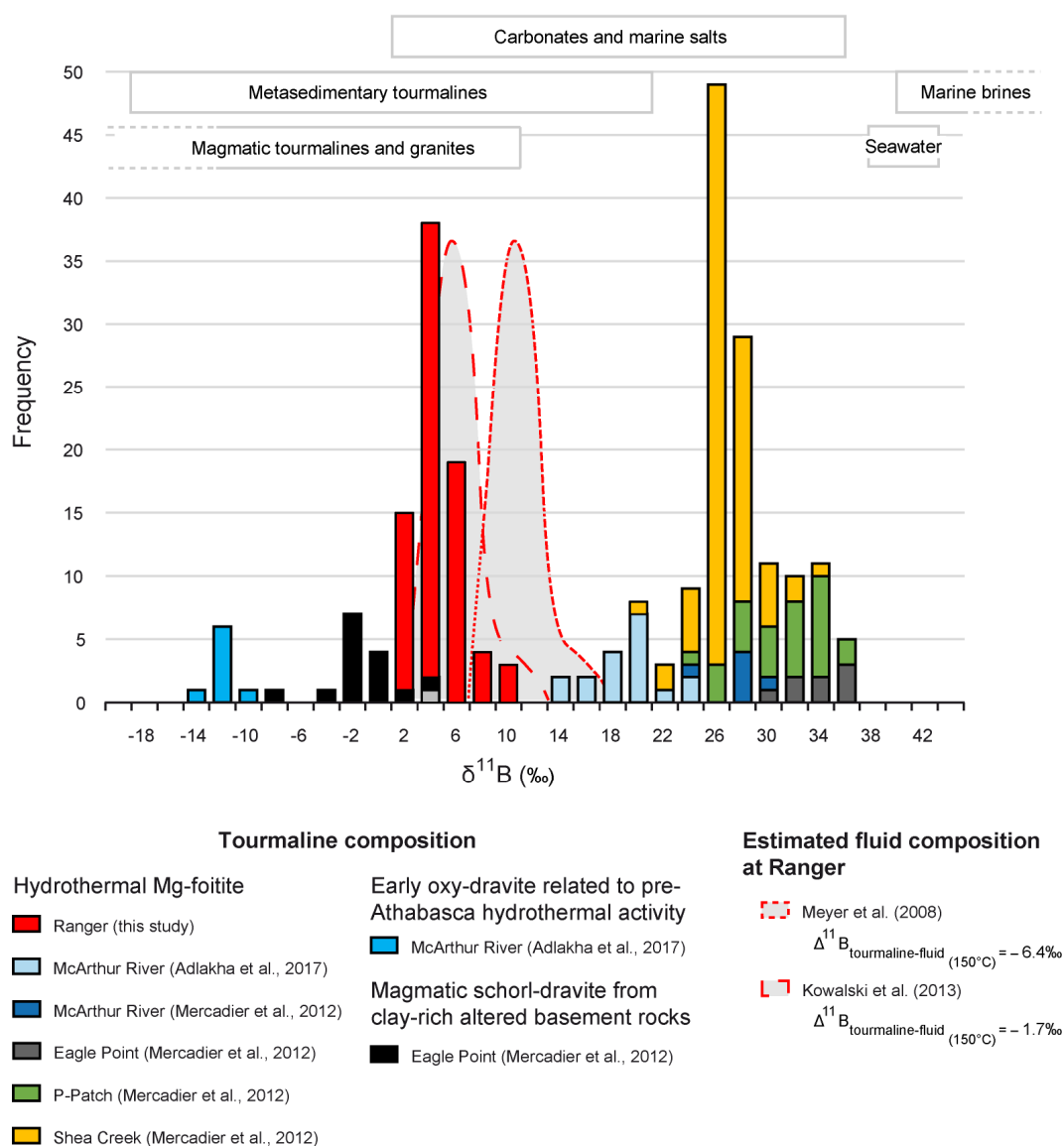


**Figure 9.** Histogram of boron isotopic compositions for tourmaline T1 at Ranger U deposit (this study) and for some of the unconformity-related U deposits from the Athabasca Basin (Canada): Adlakha et al. [32] and Mercadier et al. [33]. The boron isotopic composition for different B reservoirs are shown ([62–64] and references therein). The range of the boron isotopic composition of the calculated fluid in equilibrium with tourmaline T1 at Ranger is indicated by a grey zone limited by a red dotted line according to two independent methods: Meyer et al. [65] and Kowalski et al. [66].

**Table 6.** B isotope compositions for tourmaline T1.

Analysis #	$\delta^{11}\text{B}$	$1\sigma$	Analysis #	$\delta^{11}\text{B}$	$1\sigma$	Analysis #	$\delta^{11}\text{B}$	$1\sigma$
1	1.78	0.62	27	1.80	0.41	52	4.84	0.76
2	1.15	0.37	28	2.72	0.54	53	4.34	0.91
3	1.22	1.01	29	4.41	0.50	54	4.26	0.89
4	0.58	0.70	30	2.66	0.52	55	4.81	1.07
5	2.15	1.22	31	2.92	0.49	56	2.69	0.52
6	1.70	0.53	32	2.91	0.40	57	3.45	0.37
7	1.39	0.49	33	3.66	0.38	58	6.22	0.72
8	3.19	0.58	34	3.36	0.42	59	3.37	0.41
9	2.55	1.07	35	3.17	0.46	60	3.31	0.51
10	5.40	0.85	36	1.66	1.29	61	4.67	0.52
11	3.94	0.72	37	8.09	1.78	62	6.70	1.18
12	1.73	0.49	38	4.65	0.45	63	5.77	0.91
13	3.20	0.57	39	5.45	0.51	64	7.55	0.28
14	3.61	0.39	40	5.63	0.71	65	9.38	0.60
15	3.90	0.60	41	4.73	0.40	66	8.75	0.53
16	3.62	0.97	42	4.95	0.86	67	2.67	0.40
17	4.34	0.54	43	4.88	0.51	68	0.80	0.90
18	2.02	0.51	44	4.79	0.49	69	2.50	0.52
19	1.77	0.47	45	7.42	0.61	70	3.74	0.52
20	0.82	0.66	46	4.23	0.53	71	4.66	0.48
21	2.07	0.47	47	2.84	0.85	72	3.35	0.44
22	3.47	0.59	48	3.99	0.75	73	4.34	0.52
23	3.43	0.52	49	3.59	0.43	74	1.45	0.76
24	3.31	0.55	50	3.88	0.47	75	1.93	0.52
25	3.18	0.55	51	3.97	0.35	76	3.22	0.66
26	3.13	0.52						

## 6. Discussion and Conclusions

### 6.1. Comparison between Unconformity-Related Deposits of the Alligator Rivers Uranium Field (Australia) and the Athabasca and Thelon Basins (Canada)

The retrometamorphic chlorite Chl1 from Ranger has a composition close to retrometamorphic chlorite from the Athabasca and Thelon basins characterized by a relatively low  $\text{Mg}/(\text{Mg} + \text{Fe}_{\text{tot}})$  ratio (Figure 8). This means that similar retrometamorphic conditions were encountered in the three localities. In the ARUF, the diagenetic-hydrothermal chlorite (including chlorite Chl2 from Ranger) related to the uranium ore-forming systems has a composition intermediate between clinocllore and Mg-amesite, with  $\text{VI}\text{R}^{3+}$  values between  $\sim 1.3$  and  $1.8$  *apfu* and  $\text{Mg}/(\text{Mg} + \text{Fe}_{\text{tot}})$  ratio between  $\sim 0.8$  and  $0.95$ . Some paragenetically equivalent chlorites from uranium deposits of the Athabasca and Thelon basins show composition similar to chlorite from the ARUF while others tend towards a sudoitic composition with higher  $\text{VI}\text{R}^{3+}$  values up to  $\sim 3.0$  *apfu* (Figure 8A). According to Kister et al. [28] the occurrence of sudoite instead of clinocllore might reflect higher  $\text{K}^+/\text{H}^+$  and lower  $\text{Mg}^{2+}/\text{H}^+$  activity ratios in the fluids of the Athabasca and Thelon basins compared to the ARUF. However, it remains unclear why those parameters would be specifically different in the ARUF compared to Thelon and Athabasca basins. Another possibility to explain this compositional difference is that more intense fluid–rock alteration occurred in the ARUF, leading to an increase in the Mg-content of the chlorites, from sudoite ( $\sim 14$  wt.% MgO) to clinocllore ( $\sim 25$  wt.% MgO) [59]. Nonetheless, while the presence of sudoite is considered a proximal indicator for uranium mineralisation in the Athabasca and Thelon basins [19,28], it should not be targeted as such during uranium exploration in the ARUF.

The texture and chemical composition of tourmaline T1 at the Ranger U deposit is consistent with that of the U-related tourmaline found in unconformity-related U deposits from the Athabasca Basin (Canada) [31–33] (Figure 7). Collectively, U-related tourmaline has typically an alkali-deficient composition with high X-site vacancy contents ranging between  $0.66$  and  $0.85$  *apfu* (except one sample)

and low  $Fe_{tot}/(Fe_{tot} + Mg)$  ratio ranging between 0.01 and 0.15, typical of Mg-foitite composition. The  $\delta^{11}B$  values of tourmaline T1 from Ranger (0.6–9.4‰, this study) are significantly lower than those from four different unconformity-related U deposits the Athabasca Basin (ca. 14 to 35‰; Figure 9 [32,33]). The intrasample variation (9‰ at Ranger) is consistent with the largest ones measured in the Athabasca Basin [32,33]. For the McArthur River deposit, it is noteworthy that the  $\delta^{11}B$  values of Mercadier et al. [33] are shifted by  $\sim +8‰$  from those of Adlakha et al. [32]. A possible explanation for this shift between the two studies on the Athabasca Basin is that Mercadier et al. [33] did not use matrix-match standards (but elbaite standard) while dravite standards were used by Adlakha et al. [32] and in this study. It is now well documented that matrix-dependent mass fractionation during SIMS analysis of boron isotopes in tourmaline could be significant [51,67,68]. Whether the data of Mercadier et al. [33] should be corrected significantly and, if so, determining the magnitude of the correction is beyond the scope of this study. However, under the assumption that the data of Mercadier et al. [33] should be shifted by  $\sim -8‰$  (in order to align the results obtained by Mercadier et al. [33] and Adlakha et al. [32] at the McArthur River U deposit), the overall  $\delta^{11}B$  values of U-related tourmaline from unconformity-related U deposits from the Athabasca basin would be  $\sim 12$ – $28‰$ ; still significantly higher than for the Ranger deposit (0.6–9.4‰). Therefore the chemical composition of tourmaline points towards similar physical-chemical conditions for the precipitation of tourmaline in both the Ranger deposit and Canadian deposits of the Athabasca Basin. However, B isotope composition of tourmaline indicates that the sources of B or the relative contribution of different B sources were significantly distinct between the Ranger deposit and some Canadian deposits of the Athabasca Basin.

## 6.2. Insights into Boron and Magnesium Metasomatism

The Mg-driven geochemical signature of the hydrothermal alteration related to U mineralisation in the unconformity-related U deposits in the ARUF [26,59] is marked for example by the formation of Mg-chlorite Chl2 co-genetic with Mg-tourmaline T1 and early uraninite U1. Tourmaline has been reported at the Jabiluka deposit within alteration halos around mineralisation [25,30,69,70] and in the Kombolgie Sandstones of the McArthur Basin [14] and seems to be always linked in time and space with chlorite which is the main indicator of the Mg-metasomatism. The relatively constant chemical and isotopic composition of tourmaline T1 from Ranger indicates rather steady conditions (temperature, pH, eH and fluid composition) during tourmaline precipitation. Analysis of tourmaline T1 and chlorite Chl2 allows determining some of the characteristics of the U-ore-forming fluid that is also related to B-Mg-metasomatism.

As tourmaline T1 formed after chlorite Chl2 and before quartz Q2, the crystallisation temperature of these two minerals can help bracketing the temperature of formation of the tourmaline T1. Here, the calculated range of temperature for chlorite Chl2 is 101–163 °C ( $128 \pm 18$  °C). These estimates should be considered with caution because Chl2 precipitated during the pre-ore B1 breccia episode during which quartz dissolution is also noted (Figure 3), while the geothermometer of Bourdelle and Cathelineau [50] assumes that quartz activity is equal to 1. However, the study of primary fluid inclusions hosted in quartz Q2 at Ranger indicates a trapping temperature of  $150 \pm 20$  °C [10] compatible with the temperature determined for chlorite Chl2 which suggests that there is no significant temperature variation during the precipitation of Chl2, T1 and Q2. The  $\delta^{11}B$  values for the fluid in equilibrium with tourmaline are calculated with two different methods. Using the tourmaline-water B isotopic fractionation factor of Kowalski et al. [66] at 150 °C ( $\Delta^{11}B_{\text{tourmaline-fluid}(150\text{ °C})} = -1.7‰$ ) leads  $\delta^{11}B$  values for the fluid in equilibrium with tourmaline ranging between 2 and 11‰. Using the tourmaline-water B isotopic factor of Meyer et al. [65] extrapolated down to 150 °C ( $\Delta^{11}B_{\text{tourmaline-fluid}(150\text{ °C})} = -6.4‰$ ) leads to  $\delta^{11}B$  values estimates for the fluid between 7 and 16‰. The  $\delta^{11}B$  values for the fluid in equilibrium with tourmaline T1 overlap the  $\delta^{11}B$  range of fluids equilibrated with carbonates and evaporites and metasedimentary tourmaline and are distinct from heavier isotopic composition typical of seawater and marine brines ( $\delta^{11}B = 40$  to 70‰, Figure 9).  $\delta^{11}B$  values for tourmaline T1 are compatible with the

highest values for magmatic tourmaline from various localities worldwide including the Athabasca crystalline basement ( $\delta^{11}\text{B} < 10\text{‰}$ , Figure 9).

Adlakha et al. [32] proposed for the Athabasca Basin a model involving groundwater dissolving carbonate or evaporitic rocks and further  $^{11}\text{B}$  enrichment of the fluid through precipitation of illite due to the preferential  $^{10}\text{B}$  incorporation into illite [71], as a mechanism to achieve heavy boron ( $\delta^{11}\text{B} = 17$  to  $28\text{‰}$ ) and relatively light hydrogen ( $\delta\text{D} = -15$  to  $-65\text{‰}$ ) isotopic compositions for the fluid in equilibrium with tourmaline. Such model is however not supported by the halogen compositions (Cl, Br) of fluid inclusions in Athabasca and ARUF deposits. The latter indicate that the unconformity-related U deposits from the Athabasca Basin and the ARUF were formed by highly-saline basinal brines derived from highly-evaporated seawater (up to epsomite saturation) [9,22,23]. The dissolution of evaporites in the Athabasca Basin is probably very limited as indicated by halogens ratios [22]. In addition, low  $\delta\text{D}$  values were also measured in fluid inclusions representative of the U-forming brines in the Athabasca Basin and are consistent with seawater evaporation [72]. Brines derived from evaporation of seawater are typically enriched in B and Mg during evaporation [73] ( $[\text{Mg}] > 2 \text{ mol kg}^{-1}$ ,  $[\text{B}] > 10^{-2} \text{ mol kg}^{-1}$ ).

Therefore, the following alternative model can be proposed. NaCl-rich and/or CaCl<sub>2</sub>-rich brines, initially enriched in B and Mg during seawater evaporation and showing a highly positive  $\delta^{11}\text{B}$  value (source 1,  $\delta^{11}\text{B} > 40\text{‰}$ ) leached a light boron reservoir (source 2, neutral to negative  $\delta^{11}\text{B}$  value) in order to reach intermediate  $\delta^{11}\text{B}$  value before precipitating chlorite Chl2 and tourmaline T1. Detrital tourmaline in the basin, magmatic tourmaline from pegmatite and metamorphic tourmaline from graphitic pelitic gneiss in the basement are potential candidates for boron source 2. However, they are not altered in the pegmatite even if the pegmatites are known to be partly chloritised and sericitised as a result of interaction with the ore-forming fluids [4]. Other possible candidates for boron source 2 in crystalline basement rocks; feldspar, and biotite/muscovite that are known to contain up to 10 ppm and 200 ppm B, respectively [74], are more reactive than magmatic or detrital tourmaline and are strongly altered in the alteration halo of unconformity-related U deposits. The isotopic signature of magmatic or metamorphic feldspar and biotite/muscovite is poorly documented but it can be proposed that it is comparable with the values obtained in magmatic or metamorphic tourmaline because of the limited isotopic fractionation at high temperature [65,66]. Considering a possible seawater signature ( $\delta^{11}\text{B} \sim 40\text{‰}$ ) for source 1 and  $\delta^{11}\text{B}$  values for the source 2 ranging from  $-30$  to  $10\text{‰}$ , and a mean  $\delta^{11}\text{B}$  value of  $\sim 8\text{‰}$  for the fluid in equilibrium with T1 tourmaline, mass balance calculation indicates that source 1 may have contributed between  $\sim 0\%$  and  $55\%$  and source 2 between  $\sim 45\%$  and  $100\%$  to the fluid's total boron budget. This would indicate a significantly higher involvement of source 2 (i.e., basement rocks) in ARUF compared to the Athabasca Basin, where source 1 (seawater) is dominant.

One major difference between U deposits from ARUF and the Athabasca Basin is the involvement of a low-salinity fluid in addition to brines as observed in fluid inclusions [9,10]. However, the absence of low-salinity fluid in the Athabasca Basin indicates that it is not a necessary ingredient for tourmaline precipitation and U deposition and probably did not contribute to the B isotope signature of T1 tourmaline. Considering the similarities of host rocks, fluid composition and temperature between the ARUF and the Athabasca Basin, the present results raise the question of the influence of fluid/rock ratio and the duration of fluid/rock interaction on the respective involvement of various B sources, and therefore on the abundance and isotopic composition of hydrothermal tourmaline in unconformity-related U deposits. However, despite its relatively low abundance, hydrothermal tourmaline (alone or in combination with other hydrothermal minerals) should be worth considering as a valuable proximal indicator for uranium mineralisation.

**Author Contributions:** Conceptualization, J.G., R.G.S., A.R., J.M., and I.R.A.; Methodology, J.G., R.G.S., and J.V.; Validation, all co-authors; Formal Analysis, all co-authors; Writing—Original Draft Preparation, J.G.; Writing—Review & Editing, all co-authors; Supervision, A.R., I.R.A., J.M., and R.G.S.; Funding Acquisition, A.R. and J.M.

**Funding:** This research was funded by OSU OTELo grants to J.M. Conditions de transport des métaux dans un mégabassin protérozoïque and A.R. Transferts de fluides et métaux dans le bassin de McArthur (Australie) and a CNRS-INSU-CESSUR grant to J.M. Transferts des fluides et métaux dans les méga-bassins paléoprotérozoïques.

**Acknowledgments:** Energy Resources Australia and in particular Greg Rogers are thanked for support in sampling at the Ranger mine site. Olivier Rouer and Michel Cathelineau (GeoRessources Lab) are greatly acknowledged for support in EPMA analyses and interpretation of chlorite compositions, respectively. Ion Probe Team Nancy are greatly acknowledged for support in SIMS analyses. The comments of two anonymous reviewers greatly helped improving the manuscript.

**Conflicts of Interest:** The authors declare no conflict of interest.

## References

1. Jefferson, C.W.; Thomas, D.J.; Gandhi, S.S.; Ramaekers, P.; Delaney, G.; Brisbin, D.; Cutts, C.; Portella, P.; Olson, R.A. Unconformity-associated uranium deposits of the Athabasca Basin, Saskatchewan and Alberta. *Bull. Geol. Surv. Can.* **2007**, *588*, 23.
2. Cuney, M.; Kyser, K. *Geology and Geochemistry of Uranium and Thorium Deposits*; Mineralogical Association of Canada: Québec, QC, Canada, 2015; Volume 46, ISBN 0-921294-57-3.
3. International Atomic Energy Agency. *Unconformity-Related Uranium Deposits*; International Atomic Energy: Vienna, Austria, 2018; ISBN 978-92-0-108518-4.
4. Skirrow, R.G.; Mercadier, J.; Armstrong, R.; Kuske, T.; Deloule, E. The Ranger uranium deposit, northern Australia: Timing constraints, regional and ore-related alteration, and genetic implications for unconformity-related mineralisation. *Ore Geol. Rev.* **2016**, *76*, 463–503. [[CrossRef](#)]
5. Mercadier, J.; Cuney, M.; Cathelineau, M.; Lacorde, M. U redox fronts and kaolinisation in basement-hosted unconformity-related U ores of the Athabasca Basin (Canada): Late U remobilisation by meteoric fluids. *Miner. Depos.* **2011**, *46*, 105–135. [[CrossRef](#)]
6. Boiron, M.-C.; Cathelineau, M.; Richard, A. Fluid flows and metal deposition near basement/cover unconformity: Lessons and analogies from Pb–Zn–F–Ba systems for the understanding of Proterozoic U deposits. *Geofluids* **2010**, *10*, 270–292.
7. Chi, G.; Chu, H.; Petts, D.; Potter, E.; Jackson, S.; Williams-Jones, A. Uranium-rich diagenetic fluids provide the key to unconformity-related uranium mineralization in the Athabasca Basin. *Sci. Rep.* **2019**, *9*, 5530. [[CrossRef](#)]
8. Chi, G.; Haid, T.; Quirt, D.; Fayek, M.; Blamey, N.; Chu, H. Petrography, fluid inclusion analysis, and geochronology of the End uranium deposit, Kiggavik, Nunavut, Canada. *Miner. Depos.* **2017**, *52*, 211–232. [[CrossRef](#)]
9. Derome, D.; Cathelineau, M.; Fabre, C.; Boiron, M.-C.; Banks, D.; Lhomme, T.; Cuney, M. Paleo-fluid composition determined from individual fluid inclusions by Raman and LIBS: Application to mid-proterozoic evaporitic Na–Ca brines (Alligator Rivers Uranium Field, northern territories Australia). *Chem. Geol.* **2007**, *237*, 240–254. [[CrossRef](#)]
10. Derome, D.; Cuney, M.; Cathelineau, M.; Fabre, C.; Dubessy, J.; Bruneton, P.; Hubert, A. A detailed fluid inclusion study in silicified breccias from the Kombolgie sandstones (Northern Territory, Australia): Inferences for the genesis of middle-Proterozoic unconformity-type uranium deposits. *J. Geochem. Explor.* **2003**, *80*, 259–275. [[CrossRef](#)]
11. Kotzer, T.G.; Kyser, T.K. Petrogenesis of the Proterozoic Athabasca Basin, northern Saskatchewan, Canada, and its relation to diagenesis, hydrothermal uranium mineralization and paleohydrogeology. *Chem. Geol.* **1995**, *120*, 45–89. [[CrossRef](#)]
12. Martz, P.; Mercadier, J.; Cathelineau, M.; Boiron, M.-C.; Quirt, D.; Doney, A.; Gerbeaud, O.; De Wally, E.; Ledru, P. Formation of U-rich mineralizing fluids through basinal brine migration within basement-hosted shear zones: A large-scale study of the fluid chemistry around the unconformity-related Cigar Lake U deposit (Saskatchewan, Canada). *Chem. Geol.* **2019**, *508*, 116–143. [[CrossRef](#)]
13. Renac, C.; Kyser, T.K.; Durocher, K.; Dreaver, G.; O’connor, T. Comparison of diagenetic fluids in the Proterozoic Thelon and Athabasca Basins, Canada: Implications for protracted fluid histories in stable intracratonic basins. *Can. J. Earth Sci.* **2002**, *39*, 113–132. [[CrossRef](#)]

14. Durak, B.; Pagel, M.; Poty, B. *Températures et Salinités des Fluides au Cours des Silicifications Diagénetiques D'une Formation Gréseuse Surmontant un Gisement D'uranium du Socle: L'exemple des Grès Kombolgie (Australie)*; Comptes rendus de l'Académie des Sciences de Paris: Paris, France, 1983; pp. 571–574.
15. Richard, A.; Cathelineau, M.; Boiron, M.-C.; Mercadier, J.; Banks, D.A.; Cuney, M. Metal-rich fluid inclusions provide new insights into unconformity-related U deposits (Athabasca Basin and Basement, Canada). *Miner. Depos.* **2016**, *51*, 249–270. [[CrossRef](#)]
16. Richard, A.; Rozsypal, C.; Mercadier, J.; Banks, D.A.; Cuney, M.; Boiron, M.-C.; Cathelineau, M. Giant uranium deposits formed from exceptionally uranium-rich acidic brines. *Nat. Geosci.* **2012**, *5*, 142–146. [[CrossRef](#)]
17. Mercadier, J.; Richard, A.; Boiron, M.-C.; Cathelineau, M.; Cuney, M. Migration of brines in the basement rocks of the Athabasca Basin through microfracture networks (P-Patch U deposit, Canada). *Lithos* **2010**, *115*, 121–136. [[CrossRef](#)]
18. Richard, A.; Pettke, T.; Cathelineau, M.; Boiron, M.-C.; Mercadier, J.; Cuney, M.; Derome, D. Brine-rock interaction in the Athabasca basement (McArthur River U deposit, Canada): Consequences for fluid chemistry and uranium uptake. *Terra Nova* **2010**, 303–308. [[CrossRef](#)]
19. Grare, A.; Benedicto, A.; Mercadier, J.; Lacombe, O.; Travé, A.; Guilcher, M.; Richard, A.; Ledru, P.; Blain, M.; Robbins, J.; et al. Structural controls and metallogenic model of polyphase uranium mineralization in the Kiggavik area (Nunavut, Canada). *Miner. Depos.* **2019**, submitted.
20. Derome, D.; Cathelineau, M.; Cuney, M.; Fabre, C.; Lhomme, T.; Banks, D.A. Mixing of sodic and calcic brines and uranium deposition at McArthur River, Saskatchewan, Canada: A Raman and laser-induced breakdown spectroscopic study of fluid inclusions. *Econ. Geol.* **2005**, *100*, 1529–1545. [[CrossRef](#)]
21. Leisen, M.; Boiron, M.-C.; Richard, A.; Dubessy, J. Determination of Cl and Br concentrations in individual fluid inclusions by combining microthermometry and LA-ICPMS analysis: Implications for the origin of salinity in crustal fluids. *Chem. Geol.* **2012**, *330*, 197–206. [[CrossRef](#)]
22. Richard, A.; Kendrick, M.A.; Cathelineau, M. Noble gases (Ar, Kr, Xe) and halogens (Cl, Br, I) in fluid inclusions from the Athabasca Basin (Canada): Implications for unconformity-related U deposits. *Precambrian Res.* **2014**, *247*, 110–125. [[CrossRef](#)]
23. Richard, A.; Banks, D.A.; Mercadier, J.; Boiron, M.-C.; Cuney, M.; Cathelineau, M. An evaporated seawater origin for the ore-forming brines in unconformity-related uranium deposits (Athabasca Basin, Canada): Cl/Br and  $\delta^{37}\text{Cl}$  analysis of fluid inclusions. *Geochim. Cosmochim. Acta* **2011**, *75*, 2792–2810. [[CrossRef](#)]
24. Richard, A.; Cauzid, J.; Cathelineau, M.; Boiron, M.-C.; Mercadier, J.; Cuney, M. Synchrotron XRF and XANES investigation of uranium speciation and element distribution in fluid inclusions from unconformity-related uranium deposits. *Geofluids* **2013**, *13*, 101–111. [[CrossRef](#)]
25. Nutt, C.J. Chloritization and associated alteration at the Jabiluka unconformity-type uranium deposit, Northern Territory, Australia. *Can. Mineral.* **1989**, *27*, 41–58.
26. Fisher, L.A.; Cleverley, J.S.; Pownceby, M.; MacRae, C. 3D representation of geochemical data, the corresponding alteration and associated REE mobility at the Ranger uranium deposit, Northern Territory, Australia. *Miner. Depos.* **2013**, *48*, 947–966. [[CrossRef](#)]
27. Earle, S.A.M.; Sopuck, V.J. Regional litho-geochemistry of the eastern part of the Athabasca Basin uranium province, Saskatchewan, Canada. In *Uranium Resources and Geology of North America*; Muller-Kahle, E., Ed.; International Agency of Nuclear Energy: Vienna, Austria, 1989; Volume TECHDOC-500, pp. 263–269.
28. Kister, P.; Vieillard, P.; Cuney, M.; Quirt, D.; Laverret, E. Thermodynamic constraints on the mineralogical and fluid composition evolution in a clastic sedimentary basin: The Athabasca Basin (Saskatchewan, Canada). *Eur. J. Mineral.* **2005**, *17*, 325–341. [[CrossRef](#)]
29. Kister, P.; Laverret, E.; Quirt, D.; Cuney, M.; Mas, P.P.; Beaufort, D.; Bruneton, P. Mineralogy and geochemistry of the host-rock alterations associated with the Shea Creek unconformity-type uranium deposits (Athabasca Basin, Saskatchewan, Canada). Part 2. Regional-scale spatial distribution of the Athabasca Group sandstone matrix minerals. *Clays Clay Miner.* **2006**, *54*, 295–313. [[CrossRef](#)]
30. Polito, P.A.; Kyser, T.K.; Thomas, D.; Marlatt, J.; Drever, G. Re-evaluation of the petrogenesis of the Proterozoic Jabiluka unconformity-related uranium deposit, Northern Territory, Australia. *Miner. Depos.* **2005**, *40*, 257–288. [[CrossRef](#)]
31. Adlakha, E.E.; Hattori, K. Paragenesis and composition of tourmaline types along the P2 Fault and McArthur River uranium deposit, Athabasca Basin, Canada. *Can. Mineral.* **2016**, *54*, 661–679. [[CrossRef](#)]

32. Adlakha, E.E.; Hattori, K.; Davis, W.J.; Boucher, B. Characterizing fluids associated with the McArthur River U deposit, Canada, based on tourmaline trace element and stable (B, H) isotope compositions. *Chem. Geol.* **2017**, *466*, 417–435. [[CrossRef](#)]
33. Mercadier, J.; Richard, A.; Cathelineau, M. Boron-and magnesium-rich marine brines at the origin of giant unconformity-related uranium deposits:  $\delta^{11}\text{B}$  evidence from Mg-tourmalines. *Geology* **2012**, *40*, 231–234. [[CrossRef](#)]
34. Marschall, H.R.; Jiang, S.-Y. Tourmaline Isotopes: No Element Left Behind. *Elements* **2011**, *7*, 313–319. [[CrossRef](#)]
35. Energy Resources of Australia Ltd. *Annual Statement of Reserves and Resources*; Energy Resources of Australia Ltd.: Darwin, Australia, 2011.
36. Lally, J.H.; Bajwah, Z. *Uranium Deposits of the Northern Territory*; Northern Territory Geological Survey: Darwin, Australia, 2006.
37. International Atomic Energy Agency. *Geological Classification of Uranium Deposits and Description of Selected Examples*; International Atomic Energy Agency: Vienna, Austria, 2018; ISBN 978-92-0-101618-8.
38. Worden, K.; Carson, C.; Scrimgeour, I.; Lally, J.; Doyle, N. A revised Palaeoproterozoic chronostratigraphy for the Pine Creek Orogen, northern Australia: Evidence from SHRIMP U–Pb zircon geochronology. *Precambrian Res.* **2008**, *166*, 122–144. [[CrossRef](#)]
39. Hollis, J.A.; Carson, C.J.; Glass, L.M. SHRIMP U–Pb zircon geochronological evidence for Neoproterozoic basement in western Arnhem Land, northern Australia. *Precambrian Res.* **2009**, *174*, 364–380. [[CrossRef](#)]
40. Hollis, J.A.; Glass, L.M.; Carson, C.J.; Armstrong, R.; Yaxley, G.M.; Kemp, A.I.S.; Phillips, D. The Geological Evolution of the Pine Creek Orogen: New pieces in the Puzzle on Orogen and Craton Scale. In Proceedings of the Annual Geoscience Exploration Seminar (AGES), Alice Springs, Australia, 20–21 March 2011; Volume 18.
41. Hollis, J.A.; Wygralak, A.S. A review of the geology and uranium, gold and iron ore deposits of the Pine Creek Orogen. *Episodes* **2012**, *35*, 264–272.
42. Annesley, I.R.; Madore, C.; Kwok, Y.Y.; Kamo, S.L.; Troy, A.; Hughes, L. U–Pb geochronology and petrochemistry of late Barramundi pegmatites from the Ranger U deposit, Northern Territory, Australia. In *Uranium Deposits: From Their Genesis to Their Environmental Aspect, Proceedings of the International Workshop “Uranium Deposits: From Their Genesis to their Environmental Aspects”, Uranium, Prague, 10–11 September 2002*; Czech Geological Survey: Prague, Czech Republic, 2002.
43. Potma, W.; Fisher, L.; Schaubs, P.; Cleverley, J.; Corbel, S.; Lau, I.; Phang, C.; Hough, R. *JSU–ERA Ranger Mineral System Project Final Report. CSIRO National Research Flagships, Minerals Down under*; Northern Territory Geological Survey: Darwin, Australia, 2012.
44. Pevely, S.; Hinman, M.; McLellan, A. Ranger 3 Deeps uranium deposit. In *Australian Ore Deposits*; Phillips, N., Ed.; Australasian Institute of Mining and Metallurgy: Carlton, Australia, 2017; pp. 461–464.
45. Energy Resources of Australia Ltd. *Ranger 3 Deeps Exploration Decline Project—Further Underground Drilling Results Released*; Energy Resources of Australia Ltd.: Darwin, Australia, 2014.
46. Polito, P.A.; Kyser, T.K.; Marlatt, J.; Alexandre, P.; Bajwah, Z.; Drever, G. Significance of alteration assemblages for the origin and evolution of the Proterozoic Nabarlek unconformity-related uranium deposit, Northern Territory, Australia. *Econ. Geol.* **2004**, *99*, 113–139.
47. Kyser, K.; Hiatt, E.; Renac, C.; Durocher, K.; Holk, G.; Deckart, K. Diagenetic fluids in Paleo- and Meso-Proterozoic sedimentary basins and their implications for long protracted fluid histories. *Mineral. Assoc. Can. Short Course* **2000**, *28*, 225–262.
48. Yavuz, F.; Karakaya, N.; Yildirim, D.K.; Karakaya, M.Ç.; Kumral, M. A Windows program for calculation and classification of tourmaline-supergrupp (IMA-2011). *Comput. Geosci.* **2014**, *63*, 70–87. [[CrossRef](#)]
49. Henry, D.J.; Novak, M.; Hawthorne, F.C.; Ertl, A.; Dutrow, B.L.; Uher, P.; Pezzotta, F. Nomenclature of the tourmaline-supergrupp minerals. *Am. Mineral.* **2011**, *96*, 895–913. [[CrossRef](#)]
50. Bourdelle, F.; Cathelineau, M. Low-temperature chlorite geothermometry: A graphical representation based on a  $T\text{--}R^{2+}\text{--Si}$  diagram. *Eur. J. Mineral.* **2015**, *27*, 617–626. [[CrossRef](#)]
51. Chaussidon, M.; Albarède, F. Secular boron isotope variations in the continental crust: An ion microprobe study. *Earth Planet. Sci. Lett.* **1992**, *108*, 229–241. [[CrossRef](#)]
52. Spivack, A.J. Boron Isotope Geochemistry. Unpublished Ph.D. Thesis, Massachusetts Institute of Technology, Cambridge, MA, USA, 1986.

53. Dyar, M.D.; Wiedenbeck, M.; Robertson, D.; Cross, L.R.; Delaney, J.S.; Ferguson, K.; Francis, C.A.; Grew, E.S.; Guidotti, C.V.; Hervig, R.L. Reference minerals for the microanalysis of light elements. *Geostand. Newsl.* **2001**, *25*, 441–463. [[CrossRef](#)]
54. Leeman, W.P.; Tonarini, S. Boron isotopic analysis of proposed borosilicate mineral reference samples. *Geostand. Newsl.* **2001**, *25*, 399–403. [[CrossRef](#)]
55. Catanzaro, E.J. *Boric Acid: Isotopic and Assay Standard Reference Materials*; National Bureau of Standards, Institute for Materials Research: Washington, DC, USA, 1970; Volume 260.
56. Rosenberg, P.E.; Foit Jr, F.F. Magnesiofoitite from the uranium deposits of the Athabasca Basin, Saskatchewan, Canada. *Can. Mineral.* **2006**, *44*, 959–965. [[CrossRef](#)]
57. Wiewióra, A.; Weiss, Z. Crystallochemical classifications of phyllosilicates based on the unified system of projection of chemical composition: II. The chlorite group. *Clay Miner.* **1990**, *25*, 83–92. [[CrossRef](#)]
58. Plissart, G.; Féménias, O.; Măruntiu, M.; Diot, H.; Demaiffe, D. Mineralogy and geothermometry of gabbro-derived listvenites in the Tisovita–Iuti ophiolite, Southwestern Romania. *Can. Mineral.* **2009**, *47*, 81–105. [[CrossRef](#)]
59. Beaufort, D.; Patrier, P.; Laverret, E.; Bruneton, P.; Mondy, J. Clay alteration associated with Proterozoic unconformity-type uranium deposits in the East Alligator Rivers uranium field, Northern Territory, Australia. *Econ. Geol.* **2005**, *100*, 515–536. [[CrossRef](#)]
60. Billault, V.; Beaufort, D.; Patrier, P.; Petit, S. Crystal chemistry of Fe-sudoites from uranium deposits in the Athabasca Basin (Saskatchewan, Canada). *Clays Clay Miner.* **2002**, *50*, 70–81. [[CrossRef](#)]
61. Martz, P. Caractéristiques, Chronologie et Rôles des Circulations Fluides dans le Bassin D’athabasca et Son Socle: Implications dans la Formation et L’évolution du Gisement D’uranium de Cigar Lake. Unpublished Ph.D. Thesis, Université de Lorraine, Nancy, France, 2017.
62. Vengosh, A.; Starinsky, A.; Kolodny, Y.; Chivas, A.R.; Raab, M. Boron isotope variations during fractional evaporation of sea water: New constraints on the marine vs. nonmarine debate. *Geology* **1992**, *20*, 799. [[CrossRef](#)]
63. Barth, S. Boron isotope variations in nature: A synthesis. *Geol. Rundsch.* **1993**, *82*, 640–651. [[CrossRef](#)]
64. Palmer, M.R.; Swihart, G.H. Boron isotope geochemistry; an overview. *Rev. Mineral. Geochem.* **1996**, *33*, 709–744.
65. Meyer, C.; Wunder, B.; Meixner, A.; Romer, R.L.; Heinrich, W. Boron-isotope fractionation between tourmaline and fluid: An experimental re-investigation. *Contrib. Mineral. Petro.* **2008**, *156*, 259–267. [[CrossRef](#)]
66. Kowalski, P.M.; Wunder, B.; Jahn, S. Ab initio prediction of equilibrium boron isotope fractionation between minerals and aqueous fluids at high P and T. *Geochim. Cosmochim. Acta* **2013**, *101*, 285–301. [[CrossRef](#)]
67. Molnár, F.; Mänttari, I.; O’Brien, H.; Lahaye, Y.; Pakkanen, L.; Johanson, B.; Käpyaho, A.; Sorjonen-Ward, P.; Whitehouse, M.; Sakellaris, G. Boron, sulphur and copper isotope systematics in the orogenic gold deposits of the Archaean Hattu schist belt, eastern Finland. *Ore Geol. Rev.* **2016**, *77*, 133–162. [[CrossRef](#)]
68. MacGregor, J.; Grew, E.S.; De Hoog, J.C.; Harley, S.L.; Kowalski, P.M.; Yates, M.G.; Carson, C.J. Boron isotopic composition of tourmaline, prismatic, and grandidierite from granulite facies paragneisses in the Larsemann Hills, Prydz Bay, East Antarctica: Evidence for a non-marine evaporite source. *Geochim. Cosmochim. Acta* **2013**, *123*, 261–283. [[CrossRef](#)]
69. Binns, R.A.; Ayres, D.E.; Wilmshurst, J.R.; Ramsden, A.R. Petrology and geochemistry of alteration associated with uranium mineralization at Jabiluka, Northern Territory, Australia. In *Uranium in the Pine Creek Geosyncline*; IAEA: Vienna, Austria, 1980.
70. Polito, P.A.; Kyser, T.K.; Alexandre, P.; Hiatt, E.E.; Stanley, C.R. Advances in understanding the Kombolgie Subgroup and unconformity-related uranium deposits in the Alligator Rivers Uranium Field and how to explore for them using litho-geochemical principles. *Aust. J. Earth Sci.* **2011**, *58*, 453–474. [[CrossRef](#)]
71. Williams, L.B.; Hervig, R.L.; Holloway, J.R.; Hutcheon, I. Boron isotope geochemistry during diagenesis. Part. I. Experimental determination of fractionation during illitization of smectite. *Geochim. Cosmochim. Acta* **2001**, *65*, 1769–1782. [[CrossRef](#)]
72. Richard, A.; Boulvais, P.; Mercadier, J.; Boiron, M.-C.; Cathelineau, M.; Cuney, M.; France-Lanord, C. From evaporated seawater to uranium-mineralizing brines: Isotopic and trace element study of quartz–dolomite veins in the Athabasca system. *Geochim. Cosmochim. Acta* **2013**, *113*, 38–59. [[CrossRef](#)]

73. Fontes, J.C.; Matray, J.M. Geochemistry and origin of formation brines from the Paris Basin, France: 1. Brines associated with Triassic salts. *Chem. Geol.* **1993**, *109*, 149–175. [[CrossRef](#)]
74. London, D.; Morgan, G.B.; Wolf, M.B. Boron in granitic rocks and their contact aureoles. *Boron* **1996**, *33*, 299–330.



© 2019 by the authors. Licensee MDPI, Basel, Switzerland. This article is an open access article distributed under the terms and conditions of the Creative Commons Attribution (CC BY) license (<http://creativecommons.org/licenses/by/4.0/>).